PROGRESS REPORT

December 1, 1978 - November 30, 1979

Contract No. EY-76-S-02-2172

MECHANICAL PROPERTIES OF CRYSTALLINE SOLIDS

by

Che-Yu Li, Professor

and

E. W. Hart, Professor

Department of Materials Science and Engineering
Cornell University
Ithaca, New York 14853

September 1, 1979

DISCLAIMER

SUMMARY

The work performed during the past fiscal year included:

1. The development and preliminary experimental verification of a second generation deformation model based on state variables, which more correctly represents transient deformation.
2. The establishment of experimental capabilities for investigating grain boundary anelasticity and the development of unified phenomenological models for grain boundary anelasticity and grain boundary sliding.
3. The continued investigation of grain boundary cavitation processes in the Zircaloys.
4. The theoretical modeling of stress relaxation in thin films.

TABLE OF CONTENTS

INTRODUCTION

The work performed during the past year is part of a continued effort at Cornell University to establish a state variable description of non-elastic deformation and related phenomena in crystalline solids and to develop applications to mechanical design.

In our previous progress report[1] we reviewed our accomplishments up to that time and discussed areas where future research was required. An important area of interest is the description of deformation processes in the grain matrix by using the state variable approach. As a result of our past work, we are able at present to use a phenomenological model proposed by Hart[2] to describe a variety of phenomena such as creep, tensile deformation, and load relaxation under conditions where plastic deformation in the grain matrix is controlling. Hart's model has been shown however, to be inadequate for some phenomena associated with transient deformation resulting from a stress or strain rate change. These phenomena include microplastic effects which occur during tensile deformation at stresses below plastic yielding, and the Bauschinger effect, which produces early yielding upon reverse loading. We have been concerned with these problems without significant success during the past three years in our research sponsored by NSF. The NSF project was terminated last fall. We have continued to work in this area under the DOE project.

In our previous progress report,[1] we also discussed the required work related to deformation processes associated with grain sliding. Specifically, we are interested in the characterization of grain boundary anelasticity as well as plastic deformation produced by grain boundary sliding. For grain boundary anelasticity, we have adopted the concept introduced by Zener[3] and his coworkers. Grain boundary shear on a macroscopic scale is thought to be always accompanied by grain matrix deformation at grain boundary steps and corners

which is required for accommodation. When the extent of grain boundary shear is limited and the time scale is short, the grain matrix deformation required for accommodation will essentially be elastic and anelastic. Once the applied stress is removed, the stored elastic and anelastic strain will provide a driving force for reversed grain boundary shear as originally proposed by Zener et al. When the extent of grain boundary shear is large and the time scale is long, the grain matrix deformation required for accommodation will include plastic deformation. Upon the removal of the applied stress the portion of the grain boundary shear which is accommodated by grain matrix plastic deformation will not recover.

The physical picture presented above suggests, as discussed in our previous progress report, the possibility of developing a unified description of grain boundary anelasticity and plastic deformation produced by grain boundary sliding such that they differ only in the way in which they are accommodated. Advances in this area has been hindered, however, by a lack of experimental capabilities, especially in the characterization of the flow properties of grain boundary sliding. For example, grain boundary anelasticity is traditionally investigated by using the internal friction technique, which yields information only on the magnitude of the relaxed modulus.

We have made significant progress during the past fiscal year in both of the areas discussed above. We have proposed a second generation phenomenological model for deformation processes in the grain matrix. The new model reduces to Hart's model when plastic deformation predominates. It has been shown experimentally to be able to describe a variety of phenomena associated with transient deformation.

In the area of grain boundary sliding we have developed the capability of characterizing grain boundary anelasticity by performing constant extension rate tensile tests at elevated temperatures and at stresses below the yield

stress. This experiment allows the determination of the magnitude of grain boundary anelasticity as well as the flow properties of the grain boundary at low stress levels. We can also perform load relaxation experiments in both the plastic and anelastic range which will provide the flow behavior of the grain boundary at higher stresses.[5] Based on preliminary experimental results, we have proposed unified phenomenological models for grain boundary anelasticity and for plastic deformation produced by grain boundary sliding. The materials parameters and the flow equation required by these models can be determined by the experiments described above. We are therefore in an excellent position as a result of the work of the past year to make a significant advance in characterizing deformation produced by grain boundary sliding.

In the following we shall report our progress on transient deformation and on grain boundary sliding in two separate sections. We shall describe our work on grain boundary cavitation processes in the Zircaloys in the third section and in the fourth section we shall discuss stress relaxation in thin films. Both of the last two topics are of current technological interest and represent a part of our effort to produce information which will find practical application in the near term.

During the past year we have also continued to contribute expertise resulting from our work to a variety of projects in national laboratories and in industry. For example we have participated in the work on thermal stress in the first wall of a fusion reactor (Argonne), the tube burst problem related to LMFBR safety and fuel element modeling (Argonne and Hanford), the characterization of the Zircaloys (EPRI), the characterization of Cr-Mo steels for steam turbines (G.E.), and the stress relaxation in lead thin films (IBM). Some of the work described above is expected to generate reports in the open literature.

The technical reports produced in the past year are listed below.

1. "The Growth of Grain Boundary Cavities under Applied Stress and In-

ternal Pressure," J. F. Maricubo and Che-Yu Li, Accepted for publication in Metl. Trans.

2. "Stress Relaxation and Hillock Growth in Thin Films," M. S. Jackson and Che-Yu Li, submitted to Acta Met.
3. "A Phenomenological Model for Transient Deformation Based on State Variables," M. S. Jackson, C. W. Cho, P. Alexopoulos, H. Mughrabi and Che-Yu Li, submitted to Acta Met.

A PHENOMENOLOGICAL MODEL FOR TRANSIENT DEFORMATION

In this section we shall first introduce the physical basis for the new model for deformation processes in the grain matrix. We shall use the new model and the model proposed by Hart[2] to simulate a variety of deformation phenomena with materials parameters of the same value and examine their differences. We shall report some of our preliminary effort to determine the materials parameters and flow equations required by the new model and to verify its validity experimentally.

1. Physical Basis

The physical basis of the new model can be introduced by first examining some of the concepts based on which the deformation model originally proposed by Hart was developed. In Figure 1a a schematic representation of Hart's model is shown.[1] The three elements a, $\dot{\alpha}$ and $\dot{\varepsilon}$ of the model represent three mechanisms of interest. The a-element is an anelastic spring. The magnitude of the anelastic strain a, measures the stored strain resulting from dislocation bowing and pile-up. The stress corresponding to this stored strain can cause plastic deformation, which is represented by the $\dot{\alpha}$-element. The rate at which the dislocation pile-up is accumulated or recovered is governed by the $\dot{\varepsilon}$-element, a glide friction element which may also modify the rate of plastic flow.

An implicit assumption of Hart's model is the existence of barriers to dislocation motion of uniform strength. For a well annealed specimen dislocation are randomly distributed between the barriers as shown in Figure 1b. According to Hart's model, under an applied stress dislocations will pile-up against the barrier resulting in anelastic strain a and a force on the leading dislocation which depends on the anelastic stress σ_a. If the value of σ_a is significantly less than the value of the hardness parameter σ^*, which is a mea-

sure of the barrier strength,[1] the rate of plastic deformation is controlled by the $\dot{\alpha}$-element (dislocation climb). As the applied stress is increased and σ_a approaches σ^*, the resistance of the $\dot{\alpha}$-element approaches zero and plastic deformation will be controlled by the $\dot{\varepsilon}$-element. The $\dot{\alpha}$-element and $\dot{\varepsilon}$-element, together with a state variable based work hardening function, have been shown to describe satisfactorily a variety of phenomena such as creep, tensile deformation and load relaxation under conditions where plastic deformation in the grain matrix predominates.[6]

Hart's model through the a-element[2] will produce non-elastic transient deformation during a constant extension rate tensile test and the Bauschinger effect upon reverse loading (Figures 3, 4 and 5). The magnitude of the predicted effects has been found however, in general to be significantly less than that observed experimentally. Qualitatively the physical picture of a distribution of barriers of uniform strength represented by Figure 1b cannot produce the microplastic phenomena which are often observed.[7] It is reasonable, however, to expect that barriers to dislocation motion in a polycrystalline solid will have a distribution of strength as represented by Figure 2b. For example, the stronger barriers can be identified as cell walls. Within them a variety of dislocation tangles are weaken barriers. The physical picture represented by Figure 2b is the basis on which the new deformation model is developed.

A schematic representation of the new deformation model is shown in Figure 2a. Since the picture of glide friction is unchanged the $\dot{\varepsilon}$-element in Figures 1a and 2a are equivalent. Similarly, the $\dot{\alpha}_1$-element of the new model is the same in the $\dot{\alpha}$-element in Hart's model. The flow properties of the $\dot{\alpha}_2$-element are governed by a hardness parameter σ_1^*, which measures the strength of the hard barriers as σ^* does in Hart's theory.

The a-element in Figure 1a is considerably modified, however, since

the dislocation pile-up process is different in the presence of weak barriers. As suggested by Figure 2b, anelastic strain can occur both by pile-up against the small barriers and by long-range pile-up restrained by the strong barriers. Since the stress-strain relationship for these two processes are different, the anelastic elements are required. In addition, dislocation motion through two small barriers will lead to microplastic strain, and a flow element is needed to represent this process.

The arrangement of these elements is also dictated by physical considerations. For example, leakage of dislocations through the small barriers will increase the long-range pile-up. This can be arranged by putting the two elements in parallel. In addition, the net force for small barrier penetration does not depend solely in the stress associated with small pile-ups, since the stress due to the long-range pile-up will resist such leakage.

These considerations are incorporated in Figure 2a. Here the a_1-element represents anelasticity due to long-range pile-ups against the strong barriers. Anelasticity due to pile-ups between weak barriers is represented by the combinaton of the a_1- and a_2-elements. The net force on the microplastic flow element $\dot{\alpha}_2$ is then properly given by the a_2-element.

The operation of the new model can be described by using Figure 2b. For a well annealed specimen dislocations are distributed randomly between barriers as shown. In a constant extension rate tensile test, as the applied stress is increased dislocations will begin to pile-up against the barriers resulting in anelastic strain ($\Delta a = \Delta a_1 = \Delta a_2$), with magnitude controlled by both the a_1- and a_2-elements and a rate governed by the $\dot{\varepsilon}$-element. When the stress is increased sufficiently to activate the $\dot{\alpha}_2$-element, dislocations will overcome the weak barriers and produce micorplastic strain (α_2). As the applied stress continues to rise, eventually the $\dot{\alpha}_1$-element will begin to operate and plastic yielding occurs. During plastic yielding $\dot{\alpha}_1$ will be close to $\dot{\varepsilon}$ which is the total non-

elastic strain rate. At stress levels near plastic yielding, a major portion of the dislocations will have overcome the weak barriers and piled up against the stronger barriers. This will be represented by a large strain in the a_1-element. During unloading the weak barriers will trap most of this strain in the forward direction. Upon reverse loading, the trapped strain a_1 can be recovered at the low stress levels necessary to overcome the weak barriers, and a Bauschinger effect will result.

The constraint equations and the constitutive equations for Hart's model are described in References 1 and 5 and in our previous progress report. The equations for the new model are given below:

$$\sigma = \sigma_f + \sigma_a = \sigma_f + \sigma_{a_1} + \sigma_{a_2} \tag{1}$$

$$\dot{\varepsilon} = \dot{\alpha}_1 + \dot{a}_1 = \dot{\alpha}_1 + \dot{a}_2 + \dot{\alpha}_2 \tag{2}$$

For the a_1-element, $$\sigma_{a_1} = M_1 a_1 \tag{3}$$

For the a_2-element, $$\sigma_{a_2} = M_2 a_2 \tag{4}$$

For the $\dot{\alpha}_1$-element, $$\ln(\sigma_1^*/\sigma_a) = (\dot{\varepsilon}_1^*/\dot{\alpha}_1)^{\lambda_1} \tag{5}$$

For the $\dot{\varepsilon}$-element, $$\dot{\varepsilon} = \dot{a}^*(\sigma_f/G)^M \tag{6}$$

We are at present not certain of the exact form of the flow equation for the $\dot{\alpha}_2$-element. For the work described in this report, we have used:

For the $\dot{\alpha}_2$-element, $$\ln(\sigma_2^*/\sigma_{a_2}) = (\dot{\varepsilon}_2^*/\dot{\alpha}_2)^{\lambda_2} \tag{7}$$

where σ_f, σ_a, σ_{a_1}, σ_{a_2}, $\dot{\alpha}_1$, $\dot{\alpha}_2$, $\dot{a}_1$, and $\dot{a}_2$ are defined as shown in Figure 2a, M_1 and M_2 are the moduli for the a_1-element and a_2-element respectively, σ_1^* and σ_2^* are hardness parameters, $\dot{\varepsilon}_1^*$ and $\dot{\varepsilon}_2^*$ are rate parameters which scaled with σ^* and temperature,[1] λ_1, λ_2 are materials constants, G is shear modulus.

We require also a work-hardening function for the $\dot{\alpha}_1$-element,

$$\frac{d\ln\sigma_1^*}{dt} = \Gamma\,(\sigma_a,\sigma_1^*)\,\dot{\alpha}_1 \qquad (8)$$

and an evolution law for σ_2^* which represents the strength distribution of the weak barriers.

As σ_{a_2} increases from zero, microplastic deformation will be resisted by the very weakest barriers. We represent their strength by σ_{20}^*. As these barriers are overcome, further deformation will be resisted by increasingly strong barriers. Thus the evolution law for σ_2^* will depend on σ_{a_2} when σ_{a_2} is increasing.

When σ_{a_2} is decreasing, microplastic deformation will continue to be resisted by the strongest barriers "sampled" before the decrease began. Thus we expect σ_2^* to be constant for this case. When the sign of σ_{a_2} changes, however, the small pile-ups will once again first be able to overcome the weakest barriers.

Although the details of this process are not known a priori, a representation of the evolution of σ_2^* which may be sufficient for present purposes is

$$\left.\begin{aligned} \dot{\sigma}_2^* &= 0 && \text{for } |\sigma_{a_2}| \text{ decreasing} \\ \sigma_2^* &= \sigma_{20}^* && \text{for } |\sigma_{a_2}| \le K\,\sigma_{20}^* \\ \sigma_2^* &= \sigma_{a_2}/K && \text{for } |\sigma_{a_2}| > K\,\sigma_{20}^* \end{aligned}\right\}, \ |\sigma_{a_2}| \text{ increasing} \qquad (9)$$

where in general K may be a function of σ_{a_2}.

We note, for completeness, that the constitutive relations for the a-element, the $\dot{\alpha}$-element and the $\dot{\varepsilon}$-element of Hart's model (Figure 1a) are the same as Equatins 4, 5, 6 and 8.

2. Simulation Calculations

The results of the computer calculation to be discussed are designed to simulate the room temperature behavior of a well annealed polycrystalline

high purity (99.99+%) aluminum specimen with a moderate amount of prior plastic deformation and stored anelastic strain. A discussion of the computer program is given in Reference 6. In Figures 3, 4, 5, and 6 the results of the calculation shown are obtained by using the new model and Hart's model. For those elements which are equivalent in both models, the same value of materials parameters are used. The materials parameters are given in Table 1.

Figure 3 shows the calculated stress vs. non-elastic strain for a simulation of a constant extension rate tensile test. The test begins at stress zero and the specimen undergoes elastic deformation at low stresses with zero non-elastic strain. As stress rises, anelastic deformation begins; the two models produce the same stress—non-elastic strain curve in the anelastic range because $M_1 + M_2$ in the new model is equal to M in Hart's model. At higher stresses prior to yielding the stress-non-elastic strain curve based on Hart's model shows continued anelastic deformation while the curve based on the new model shows microplastic behavior. After yielding the two curves again show similar behavior because the $\dot{\alpha}_1$-element and the $\dot{\alpha}$-element are the same and the same work hardening function is used. We note in passing, that the difference of the two curves in the microplastic region is related to some of the controversies in the current literature concerning thermal recovery.

Figure 4 shows calculated stress-and non-elastic strain for a simulation of repeated loading and unloading in a constant extension rate tensile test with the maximum stress in the microplastic region but below plastic yielding. The stress-non-elastic strain loop calculated using Hart's model involves anelastic strain only, and therefore repeats itself upon repeated loading-unloading. The same loops based on the new model move forward in strain in agreement with experimental results and show also the expected shape.

Figure 5 shows calculated stress and non-elastic strain during simulation of a constant extension rate test for loading in compression of a specimen

which has been loaded previously into the plastic region in tension. It is seen that the stress and non-elastic strain calculated from the new model show the expected Bauschinger effect.

Figures 6a and 6b show the logarithm of stress and non-elastic strain rate calculated for load relaxation in a specimen which has been deformed into the plastic region but loaded to stress levels below plastic yielding prior to load relaxation. The calculated stress- non-elastic strain rate based on the new model, because of the $\dot{\alpha}_2$-element (microplastic), show the characteristics of load relaxation obtained in the so-called "transient" region reported by us previously.[8] The upper most curve in both Figures 6a and 6b simulates load relaxation data in the plastic region (Equation 5).

The above examples are chosen to show that Hart's model, in spite of its tremendous success in describing the plastic properties of polycrystalline solids, is inadequate for some of the deformation phenomena associated with stress or strain rate changes. These examples serve also to illustrate the capabilities of the new model to simulate a variety of transient deformation phenomena.

3. Experimental Verification

An important feature of our research on deformation is the emphasis which we have placed on experimental work. All of the constitutive equations and the required materials parameters of a proposed model have to be determined uniquely by separate experiments. The new model discussed here of course satisfies this requirement. In the following, we shall describe briefly how one can determine the flow equations and materials parameters of the new model. We shall show that the required experimental techniques include only constant extension rate tensile tests and load relaxation tests, which are less time consuming than creep and creep recovery tests. We shall show also that we can use the experimentally determined information and the new model to simulate transient defor-

mation phenomena to compare with experimental data.

It is worth noting that the development of our new model would not have been possible without the extensive transient deformation data which we collected during the past three years. These data, because of our capabilities in making precise strain measurement, are reproducible and were obtained under a wide range of experimental conditions. It is these data which provided the physical insight based on which the new model was developed.

Typical experimental data for well annealed polycrystalline high purity (99.99+%) aluminum, based on which we determined the flow equations and materials parameters for the new models are shown in Figures 7 and 8. Figure 7 shows stress vs. non-elastic strain data obtained in a constant extension rate tensile test at room temperature by loading and unloading in the stress range below plastic yielding. The slope of the data in the anelastic region yielded the value of $M_1 + M_2$ (Equations 3 and 4). The value of M_1 can be estimated from the Bauschinger effect since the amount of extra strain on reverse loading is sensitive to this parameter (Figure 5).

Figure 8 shows several sets of load relaxation data obtained at room temperature with the specimen loaded at stresses below plastic yielding. These data validated the flow equation for the $\dot{\alpha}_2$-element and yielded values of σ_2^* and $\dot{\varepsilon}_2^*$ for various points on the loading curve.

The evolution law for σ_2^* (Equation 9) was determined by using the stress-non-elastic strain data in the microplastic region (Figure 7) and the load relaxation results noted previously.

To determine the materials parameters for the $\dot{\alpha}_1$-element and the $\dot{\varepsilon}$-element we used the method developed for Hart's model by taking advantage of the load relaxation and tensile data in the plastic range.[5,6] The form of the constitutive equations for these elements (Equations 5, 6 and 8) is well established.[1,5,6]

With the materials parameters and flow equations determined as described above for high purity aluminum, we have attempted to use the new model to simulate the transient deformation behavior of the same material. Figures 9 and 10 show both the results of simulation calculation and experimental data. The dots shown in the figures are experiment data which were obtained first by loading at a constant extension rate (A → B in both figures). At point B the cross-head of the tensile machine was fixed resulting in load relaxation (B → C in both figures). We note that between B and C the stress decreased due to load relaxation with the specimen continued to deform in the forward direction.[8] We then unloaded the specimen at the same extension rate (C → D). The data shown in Figure 10 were obtained by reloading the same specimen following the sequence shown in Figure 9. It should be noted the strain change measured in these experiments was extremely small.

The solid curves in Figures 9 and 10 are results of simulation calculations. It is seen that they agree well with experimental data. In the simulation calculation we used a fixed value for $\dot{a}^*$ (the rate parameter for dislocation glide). The simulation can be improved if we vary the value of $\dot{a}^*$ as a function stress reflecting the effect of solute-dislocation interactions.

The material reported in this section covers only the highlights of our progress in this area of research. We are in the process of preparing a series of technical reports which will describe in more detail our new developments. We are also continuing our experimental work to fully characterize the constitutive equations of the new model and to test their applicability. We feel that we are in a position at present to extend the state variable approach to cover a significantly wider range of deformation phenomena.

GRAIN BOUNDARY SLIDING

In this section we shall report on progress made during the past year toward a unified description of anelastic and plastic deformation produced by grain boundary sliding. We shall first discuss various alternatives in phenomenological modeling by using the physical concept discussed in the introduction section. We shall report our experimental effort designed to test the validity of these models. A part of our accomplishments during the past year is the development of the experimental capabilities for characterizing the magnitude of grain boundary anelasticity as well as the flow properties of the grain boundary in the anelastic region.

1. Phenomenological Models

As discussed in the introduction section, grain boundary sliding and grain matrix deformation are coupled such that grain boundary sliding is always accompanied by the grain matrix deformation at grain boundary steps and corners which is required for accommodation. It is easy to visualize that both stress and strain concentration will exist at these sites.

For the purpose of developing a phenomenological description one should prefer models which incorporate as many as possible the important physical features of the phenomenon but are of a simple form. The parallel and series models proposed by Hart for describing plastic deformation produced by grain boundary sliding are examples of the phenomenological models of interest.[9] We have extended the parallel model of Hart to include grain boundary anelasticity.

Figure 11a shows a possible model based on the parallel arrangement. This model consists of two branches in parallel, the total stress is related to the stresses in the upper and lower branches (σ_1 and σ_2) by

$$\sigma = Y\sigma_1 + (1-Y)\sigma_2 \qquad (10)$$

where the parameter Y explicitly represents the stress concentration during

grain boundary sliding.

In Figure 11 the E-elements represent elastic behavior (E = Young's modulus for tensile deformation) and the M-elements represent the entire model for non-elastic deformation in the grain matrix as shown in Figure 2a. The arrangement in Figure 11a is such that when no grain boundary sliding occurs ($\dot{\varepsilon}_g$=o) the behavior reduces to that of the matrix.

The remaining three elements in the lower branch of Figure 11a represent grain boundary behavior. The $\dot{\varepsilon}_g$-element controls the sliding rate and represents the "viscosity" of the boundary.

As noted previously, sliding requires matrix accommodation. This is incorporated through the upper branch. It is possible, however, that additional accommodation processes may be necessary. These are represented by an additional grain boundary anelastic spring (M_g) which at high stress may be relaxed by grain boundary plastic flow ($\dot{\alpha}_g$-element). It is also possible that these elements can correct for any effect due to strain concentrations, which is not otherwise incorporated.

Under conditions where only anelastic deformation is operating, the M-element can be represented by the M_m-element in parallel with the $\dot{\varepsilon}$-element (Figure 2a) with $M_m = M_1 + M_2$. (Equations 3 and 4). The model given in Figure 11a can therefore be simplified as shown in Figure 11b.

According to the model in Figure 11b, in a constant extension rate tensile test, if the specimen is loaded and unloaded in the anelastic range, the resulting stress-total strain data will form a closed loop as those shown in Figures 15-21. At low temperatures, the lower stress range of the loading data will show elastic behavior. As the stress is increased, the data at higher stresses will reflect the contribution of elastic deformation and grain matrix anelastic deformation. As the temperature is increased the elastic range will be suppressed and at higher stresses, the data will exhibit the

effect of elastic deformation, grain matrix anelastic deformation and grain boundary anelastic deformation.

According to the model in Figure 11b, in the stress range where all three types of deformation are operating, the measured slope based on stress-total strain data, E'_{eff} will be

$$E'_{eff} = Y/(\frac{1}{E} + \frac{1}{M_m}) + 1-Y/(\frac{1}{E} + \frac{1}{M_m} + \frac{1}{M_g}) \qquad (11)$$

Equation 11 does not allow the determination of the value of Y and M_g uniquely based on the measured value of E'_{eff}. Equation 11 shows however, the maximum value of Y corresponds to $M_g \to o$. This is a very interesting limit. This limit suggests that the magnitude of grain boundary anelasticity as measured by E'_{eff} can be characterized only by the parameter Y in addition to E and M_m such that

$$E'_{eff} = Y/(\frac{1}{E} + \frac{1}{M_m}) \qquad (12)$$

Equation 12 is the simplest representation of the physical picture discussed previously. It corresponds to the case where strain concentration is negligible and the anelastic resistance to grain boundary sliding is entirely due to matrix behavior. For this case the $\dot{\alpha}_g$-element in Figure 11a is no longer needed and the model in Figure 11a can be simplified as shown in Figure 11c, where the $\dot{\varepsilon}_g$-element governs grain boundary sliding both for anelastic and plastic deformation. If the model in Figure 11c is applicable, we shall have a very simple and attractive phenomenological model. We require only the parameter Y and a grain boundary sliding element, the $\dot{\varepsilon}_g$-element to characterize grain boundary effects during non-elastic deformation.

The experimental work performed during the past year was designed to verify the validity of the model in Figure 11c and if necessary the one in Figure 11a which contains more grain boundary elements. It was designed also to measure the magnitude of Y and the flow characteristics of the $\dot{\varepsilon}_g$-element.

The strategy which we are taking involves the determination of the value of Y by using Equation 12 and experimental data similar to those shown in Figures 15-21 by using the strain gauge assembly shown in Figure 12. We can determine the value of Y also by using the model in Figure 11c and load relaxation data in the plastic range. For example, the load relaxation data in the plastic range, for Type 316 stainless steels at 600°C are shown in Figure 22.[1] The high stress and low stress limits of the data reflect grain matrix deformation. According to the model in Figure 11c, the difference in logrithmic stress level of the two grain matrix curves measures the value of Y. If the value of Y determined by the two approaches is the same, we can use this result to support the applicability of the simple model in Figure 11c. If not, we can use the value of Y from the load relaxation data to determine the value of M_g in Equation 11. For the latter case, we shall have to use the more complicated model in Figure 11a to describe grain boundary sliding.

To characterize the flow properties of the grain boundary sliding elements the $\dot{\varepsilon}_g$-element, we plan to perform constant extension rate tensile tests by loading and unloading the specimen in the anelastic range to obtain the stress dependence of $\dot{\varepsilon}_g$ and to perform load relaxation tests in both the anelastic and plastic range to collect additional flow data.

2. Experiments

For the experimental plan described above, we require the capabilities of making precise strain measurements (in the 10^{-6} inch range) at elevated temperatures to produce data similar to those shown in Figures 15-21. The accuracy and the ease of strain measurements at elevated temperatures have been limited in the past by the requirements of some form of extension rods in order that strain gauges or measuring devices can operate at room temperature. We have developed an elaborate extension rod system (concentric quartz tubes) for this purpose. This system provided adequate precision but was very cumbersome

to use.

During the past year we have developed an alternate strain measuring system for all temperatures. This system uses the capacitance gauges manufactured by Materials Technology Inc. and eliminates the need for extension rods. It is easier to use and is more accurate than the LVDT system which we have used for room temperature measurements. A schematic representation of the way in which capacitance gauges were attached to the tensile specimen is shown in Figure 12. The strain is measured by the change in gap distance between the capacitance probe and the target plate. We are in the process of preparing a technical report on the development of this capacitance gauge system.

Typical data obtained by using this new gauge system are shown in Figures 13-21. For these experiments we used a well annealed polycrystalline Nickel 270 specimen with some prior plastic deformation. The data in Figures 15-21 are closed stress-total strain loops resulting from loading and unloading in the anelastic range in a constant extension rate tensile test. The experimental sequence involved first loading and unloading into the microplastic range to produce an open loop (Figure 13). We then successively decreased the maximum stress during loading after each loading-unloading sequence (Figure 14) and eventually produced the closed loops in Figures 15-21. Once the satisfactory stress level was found, several closed loops were produced.

The data in Figures 15-21 were analyzed by using the model in Figure 11c and Equation 12. The results of the data analysis are given in Table II. For each temperature several loops were analyzed. The loading portion of the data is characterized by three types of behavior as indicated approximately by the three stress ranges in Table II. In the elastic range, elastic deformation predominates. The slope of the data yielded elastic moduli in good agreement with reported value. In the grain matrix anelastic range, both elastic deformation and grain matrix anelastic deformation are important. The measured

slope can be used to calculate the value of $M_m = M_1 + M_2$ as given in Table II. In the grain boundary anelastic range, elastic, grain matrix anelastic, and grain boundary anelastic deformation contribute.

The measured slope E'_{eff} and Equation 12 yielded a value of Y close to 0.9 as shown in Table II.

Qualitatively the data in Figures 15-21 exhibited the behavior expected of the models in Figures 11b and 11c. At lower temperatures only the elastic and grain matrix anelastic deformation were seen (see also Table II). At 400°C all three types of behavior were observed. At 500°C and 600°C the elastic range was suppressed.

We are in the process of performing load relaxation tests to determine if the same value of Y is applicable, as well as other experiments according to the research plan outline in the previous sub-section. We consider that the development of the experimental capabilities described above represents a major milestone in our research on grain boundary sliding. We should be able to make significant progress in this area of research in the near future.

GRAIN BOUNDARY CAVITATION

Under an applied tensile stress, the stress concentration at grain boundary steps and corners produced by grain boundary sliding will lead to the nucleation of creep cavities. These cavities will grow as a function of time as a result of stress-induced diffusion with grain boundaries being the sinks for atoms. The cavitation process is known to reduce ductility and specimen life in a creep-to-rupture test and to decrease fatigue life in a low cycle fatigue test with long hold times in tension. We are interested in the kinetics of nucleation and growth of creep cavities and in their description by using the state variable approach. We shall elaborate further the application of the state variable approach. A part of our interest in this area of research is to develop the capability of predicting more accurately the service life of a structural component at elevated temperatures.

As mentioned in our previous progress report, our research is motivated in part also by our interest in identifying the important damage processes which govern the life of the fuel element cladding of a light water reactor. Creep damage in the form of grain boundary cavities has not received much attention in the past, probably because (1) the operating temperature of a light water reactor is low on a homologous temperature scale based on the absolute melting temperature of the Zircaloys, and (2) a significant portion of thelife of the present fuel element of a light water reactor is in the so-called creep-down region where the cladding is under compressive loading.

We began the search for cavitation damage in the Zircaloys because our load relaxation studies of these materials showed evidence of grain boundary sliding at light water reactor temperatures which is a pre-requisite of grain boundary cavitation and because of the existence of a phase transformation temperature at 860°C which can shift the homologous temperature scale downward

significantly. During the past two years we have observed grain boundary cavities both in Zircaloy-4 and Zircaloy-2 specimens which have been crept at temperatures and in a stress and strain rate range of interest to light water reactor applications. A moderate amount of grain boundary cavitation such as that reported in Reference 10 has been shown to reduce significantly the ductility of the Zircaloys in a tensile test. During the past year we have continued our research on the nucleation and growth of creep cavities in the Zircaloys.

It has been reported inthe literature[10] that at an appropriate temperature, the number density of creep cavities was found to be proportional to the total strain of the specimen. The same result was observed in our work on the Zircaloys (Zr-2); recent results at two temperatures are shown in Figures 23 and 24. We have, however, found the temperature dependence of the cavity growth rate at a given stress to be less than that of the activation energy of grain boundary diffusivity (Figure 25). These results are consistent with the current concepts of grain boundary cavitation.

One can visualize that cavity nucleation will occur first at sites where the stress concentration is sufficiently high with only a small amount of grain boundary shear. As the grain boundary strain continues to increase, the stress concentration at other sites will increase eventually and also lead to cavity nucleation. Thus at a given temperature and stress the site of cavity nucleation is expected to depend on the rate of grain boundary sliding and the extent and the history of accumulation of grain boundary strain. The state variable approach, through the use of phenomenological models such as those in Figure 11, will generate the type of information described above on grain boundary sliding and provide a basis for analyzing and correlating the nucleation data for creep cavities.

In our previous work we have reported that the rate of stress induced cavity growth is not linearly dependent on applied stress as expected of simple

growth theories.[12] The observed stress dependence is rationalized to be caused by the redistribution of the stress component of the applied stress normal to the grain boundary as a result of grain boundary sliding. The temperature dependence of the cavity growth rate shown in Figure 25 is consistent with this possibility. This is because the extent of grain boundary sliding and the resulting stress redistribution will vary with temperature with an activation energy different from that for grain boundary diffusion. The state variable approach and the phenomenological models will also provide the information on grain boundary sliding relevant to cavity growth.

We are continuing our work on the nucleation and growth of grain boundary cavities in the Zircaloys. We are at the same time using the approach described in the previous section to characterize grain boundary sliding in these materials. It is expected that the experimental results obtained will provide the necessary basis for the development of kinetic equations based on state variables for grain boundary cavitation.

STRESS RELAXATION IN THIN FILMS

Thin solid films for electronic device applications are usually grown on a substrate at a temperature such that the deposition process will produce an essentially stress free film. When the temperature is later changed, the difference in the coefficients of thermal expansion of the film and the substrate can lead to large two-dimensional thermal stresses in the film.

These stresses can, of course, be relaxed to an extent by anelastic and plastic deformation processes. In the case of a lead film where room temperature is close to half of the absolute melting temperature on a homologous temperature scale, the relaxation at room temperature will involve grain boundary processes.

If the thermal stresses are tensile in nature, voids are observed to nucleate and grow in the grain boundaries. If the thermal stresses are compressive, under similar conditions, a phenomenon called hillock growth is known to occur, in which macroscopic whiskers or humps are found. These hillocks can lead, for example, to failure in multilayer devices due to shorting.

In order to estimate the rate of void or hillock growth, the stress level and its rate of relaxation in the thin films as a function of thermal history is a part of the required input information. It is difficult, however, to perform experiments on thin films directly to characterize their deformation properties. The application of the state variables approach will offer the advantage that the functional form of their constitutive equations is not expected to be influenced by the dimension of the specimen or by the way in which it is prepared. There are only a limited number of parameters, for example the hardness parameter σ^*, which will have a different value from that for a bulk specimen. If one can estimate the value of these parameters, it will be possible to calculate the rate of stress relaxation as a function of thermal history.

The investigators at IBM have reported some experimental information on

the relaxation of thermal strain as a function of time by using the X-ray techniques. We have used the reported data for one temperature to estimate the value of the hardness parameter σ^*. We have been able to use this value and our constitutive equations to calculate the rate of relaxation of thermal strain (or stress) at several other temperatures. A detailed description of this work has been included in a technical report.[13] It represents a part of our continued interest in seeking applications of our research findings.

REFERENCES

1. Progress Report, "Mechanical Properties of Crystalline Solids", December 1, 1977 - November 30, 1978, Contract No. EY-76-S-02-2172, DOE Report COO-2172-25, Cornell University, 1978.
2. E. W. Hart, J. Eng. Materials and Technology, Vol. 98, 193 (1976).
3. C. Zener, Elasticity and Anelasticity in Metals, U. of Chicago Press (1948).
4. T. S. Kê, Phys. Rev., Vol. 71, 533 (1947).
5. F. H. Huang, H. Yamada and Che-Yu Li, in Characterization of Materials for Service at Elevated Temperatures, G. V. Smith, Ed., ASME MPG-7 (1978).
6. V. Kumar, et al., "Deformation in Type 304 Stainless Steel", Final Report, RP-697-1, EPRI (1979).
7. J. M. Roberts, Acta Met., Vol. 15, 411 (1967).
8. E. W. Hart, et al., in Constitutive Equations in Plasticity, A. S. Argon, Ed., MIT Press (1975).
9. E. W. Hart, Acta Met., Vol. 15, 1545 (1967).
10. R. L. Kensseyan, C. P. Hu and Che-Yu Li, J. Nucl. Mat., Vol. 80, 390 (1979).
11. B. J. Cane, Metal Science, Vol. 12, 102 (1978).
12. J. F. Mancuso and Che-Yu Li, "The Growth of Grain Boundary Cavities Under Applied Stress and Internal Pressure", accepted for publication in Met. Trans.
13. M. S. Jackson and Che-Yu Li, "Stress Relaxation and Hillock Growth in Thin Films", submitted to Acta Met.

FIGURE CAPTIONS

Figure 1: (a) A schematic representation of Hart's model.

(b) A physical interpretation of Hart's model.

Figure 2: (a) A schematic representation of the new deformation model.

(b) A physical interpretation of the new model.

Figure 3: Computer simulation of a constant extension rate tensile test including plastic yielding, Hart's model: solid lines; the new model: dashed lines.

Figure 4: Computer simulation of loading and unloading loops below plastic yielding in a constant extension rate tensile test, Hart's model: solid lines; the new model: dashed lines.

Figure 5: Computer simulation of the Bauschinger effect. The calculations shown are for loading in compression at a constant extension rate with a specimen which has been plastically deformed in tension. Hart's model: solid lines; the new model: dashed lines.

Figure 6: Computer simulation of load relaxation in the transient region. The upper most curve is the so-called "λ curve" (Equation 5) for relaxation by plastic deformation. The remaining curves are calculated for loading below plastic yielding prior to load relaxation. Hart's model: Figure 6a; the new model: Figure 6b.

Figure 7: Experimentally determined loading-unloading stress-non-elastic strain loop for high purity aluminum at room temperature and an extension rate of 0.02 inch/min.

Figure 8: Experimentally determined transient load relaxation data similar to those shown in Figure 6 for a high purity aluminum at room temperature. The top curve is obtained in the plastic range.

Figure 9: Comparison of experimental data and computer simulation by using the new deformation model; the parameters used are those in Table I; the experimental data are discussed in the text.

Figure 10: Comparison of experimental data and computer simulation by using the new deformation model; the parameters used are those in Table I; the experimental data are discussed in the text.

Figure 11: A schematic representation of possible phenomenological models for grain boundary sliding.

Figure 12: A schematic representation of capacitance gauge and tensile specimen assembly.

Figure 13: Room temperature, stress-total strain data obtained in a constant extension rate tensile test by loading-unloading in the micro-plasticity range (high purity aluminum and an extension rate of 0.02 inch/min.).

Figure 14: Room temperature, stress-total strain data obtained in a constant extension rate tensile test by loading-unloading with less micro-plasticity compared to the data in Figure 13 with the same experimental condition.

Figure 15: Room temperature, closed stress-total strain loop obtained in a constant extension rate tensile test by loading-unloading in the anelastic range with the same experimental conditions as those for the data in Figure 13.

Figure 16: 100°C, closed stress-total strain loop obtained in a constant extension rate tensile test by loading-unloading in the anelastic range with the same experimental conditions as those for the data in Figure 13.

Figure 17: 200°C, closed stress-total strain loop obtained in a constant extension rate tensile test by loading-unloading in the anelastic

range with the same experimental conditions as those for the data in Figure 13.

Figure 18: 300°C, closed stress-total strain loop obtained in a constant extension rate tensile test by loading-unloading in the anelastic range with the same experimental conditions as those for the data in Figure 13.

Figure 19: 400°C, closed stress-total strain loop obtained in a constant extension rate tensile test by loading-unloading in the anelastic range with the same experimental conditions as those for the data in Figure 13.

Figure 20: 500°C, closed stress-total strain loop obtained in a constant extension rate tensile test by loading-unloading in the anelastic range with the same experimental conditions as those for the data in Figure 13.

Figure 21: 600°C, closed stress-total strain loop obtained in a constant extension rate tensile test by loading-unloading in the anelastic range with the same experimental conditions as those for the data in Figure 13.

Figure 22: Load relaxation data of Type 316 stainless steel at 600°C in the plastic range showing the effect of grain boundary sliding (S-shaped curve). The two dashed curves represent two limiting grain matrix controlled relaxation conditions.

Figure 23: Measured number density of creep cavities in Zr-2 at 350°C in the same plot with the creep strain of the specimen.

Figure 24: Measured number density of creep cavities in Zr-2 at 375°C in the same plot with the creep strain of the specimen.

Figure 25: Logrithmic cavity growth rate plotted vs. 1/T. The growth rate is measured based on the cross-sectional area of the cavity. Applied stress is 17.21 ksi.

TABLE IA

PARAMETERS FOR HART'S MODEL

YOUNG MODULUS	$= 8.5 \times 10^{6}$ PSI	
MACHINE COMPLIANCE	$= 3.2232 \times 10^{-5}$ (PSI^{-1})	
INITIAL LENGTH	= 1.5356 inch	
INITIAL AREA	$= 4.5338 \times 10^{-2}$ $inch^2$	
INITIAL SIGMA STAR	$= 8.7232 \times 10^{3}$ PSI	
INITIAL EPSILON DOT STAR	$= 4.7976 \times 10^{-15}$ sec^{-1}	
ANELASTIC MODULUS (M)	$= 85.5 \times 10^{6}$ PSI	
DISLOCATION GLIDE CONST ($= \frac{\dot{a}^*}{(M)^M}$)	$= 5 \times 10^{-12}$	
CAPITAL M	= 7.8 *	
SMALL M	= 4.8 *	
LAMBDA	= 0.15 *	
BETA	$= 1.50 \times 10^{4}$ *	} Work hardening parameters
DELTA	= 2.80 *	}

* As defined in Reference 6.

TABLE IB

PARAMETERS FOR NEW MODEL

YOUNG MODULUS	= 8.5×10^{6} PSI
MACHINE COMPLIANCE (VARIABLE) AT MAX	= 3.2232×10^{-5} (PSI^{-1})
INITIAL LENGTH	= 1.5856 inch
INITIAL AREA	= 4.533×10^{-2} $inch^2$

a) PARAMETERS FOR MICROPLASTIC BRANCH

SIGMA STAR 2	= 60.0 PSI
EPSILON DOT STAR 2	= 3.1995×10^{-23}
SCRIPT M 2	= 69.2×10^{6} PSI for scaling between σ_2^* and $\dot{\varepsilon}_2^*$
LAMBDA 2	= 0.15
SMALL M 2	= 7.2598
INITIAL SIGMA A2	= -1.725×10^{3} PSI
K = SIGMA A2/SIGMA STAR 2 Evolution law for micro-plastic element.	= $\exp(-\frac{\sigma_{a_2}}{\sigma_1^*} \frac{M_2}{M_1+M_2})$

b) PARAMETERS FOR MACROPLASTIC ELEMENT

INITIAL SIGMA STAR 1	= 8.7232×10^{3} PSI
INITIAL EPSILON DOT STAR	= 4.7976×10^{-16} sec^{-1}
SCRIPT M 1	= 16.3×10^{6} PSI
LAMBDA 1	= 0.15
SMALL M 1	= 4.8 for scaling with σ_1^{*6}
INITIAL SIGMA A2	= 2.1957×10^{3} PSI
BETA	= 1.5×10^{4} * } Work hardening parameters
DELTA	= 2.8 * }
DISLOCATION GLIDE CONST	= 5.0×10^{-12}

* As defined in Reference 6.

TABLE II

RESULTS OF DATA ANALYSIS FOR FIGURES 15-21

Temp. (°C)	Elastic Range (ksi)	E	Grain Matrix Anelastic Range (Slope = E_{eff}) (ksi)	E_{eff}	M_m	Grain Boundary Anelastic Range (Slope = E'_{eff}) (ksi)	E'_{eff}	Y
24	0-9.25	29.48	9.25-18.40	28.125	611.3	NA	NA	NA
100	0-8.70	29.25	8.70-17.9	27.37	472	NA	NA	NA
200	0-7.38	28.82	7.38-14.43	26.97	380.3	NA	NA	NA
300	0-5.38	28.78	5.38-11.25	24.90	184	NA	NA	NA
400	0-3.88	26.96	3.88-8.81	22.98	121.98	8.81-10.8	21.17	.92
500	Non-observable	25.05*	0-4.12	20.49	119.57	4.12-7.11	18.56	.9
600	"	24.48*	0-2.53	20.32	112.56	2.53-5.63	18.20	.89

* Literature value.

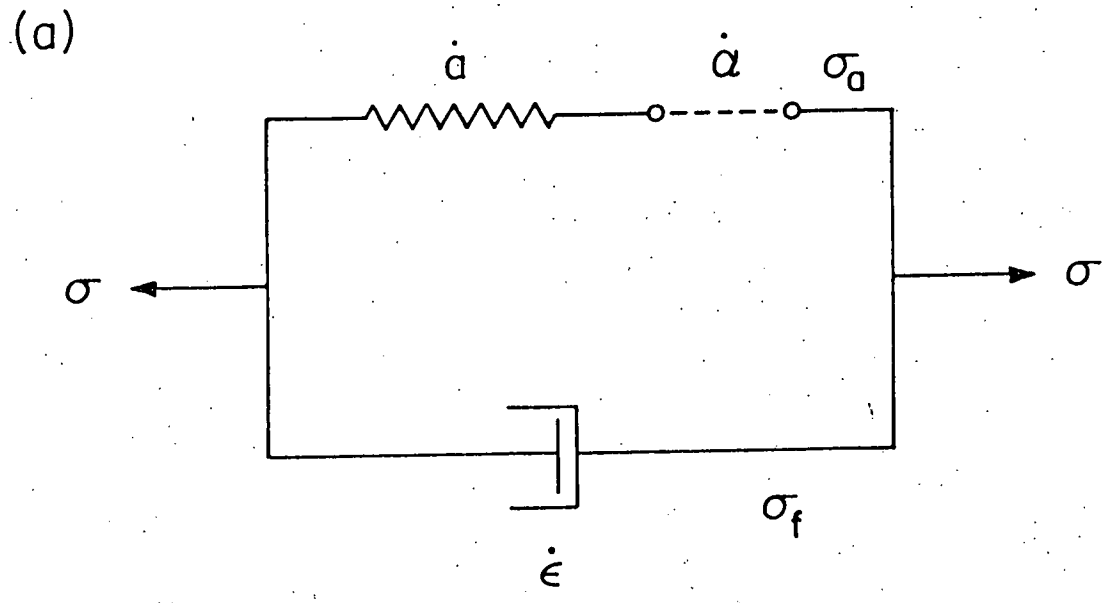

Figure 1: (a) A schematic representation of Hart's model.

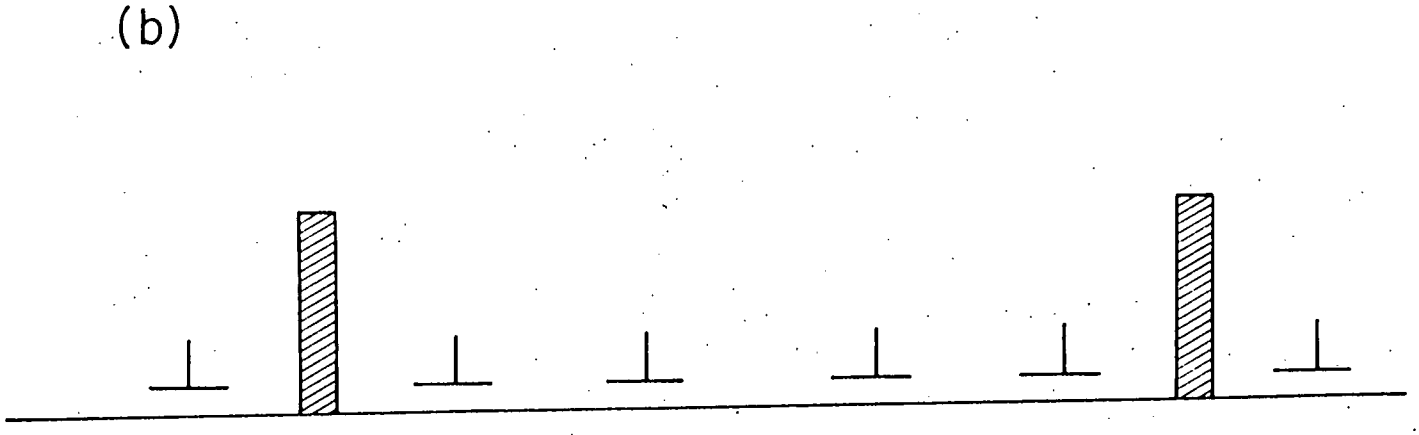

Figure 1: (b) A physical interpretation of Hart's model.

(a)

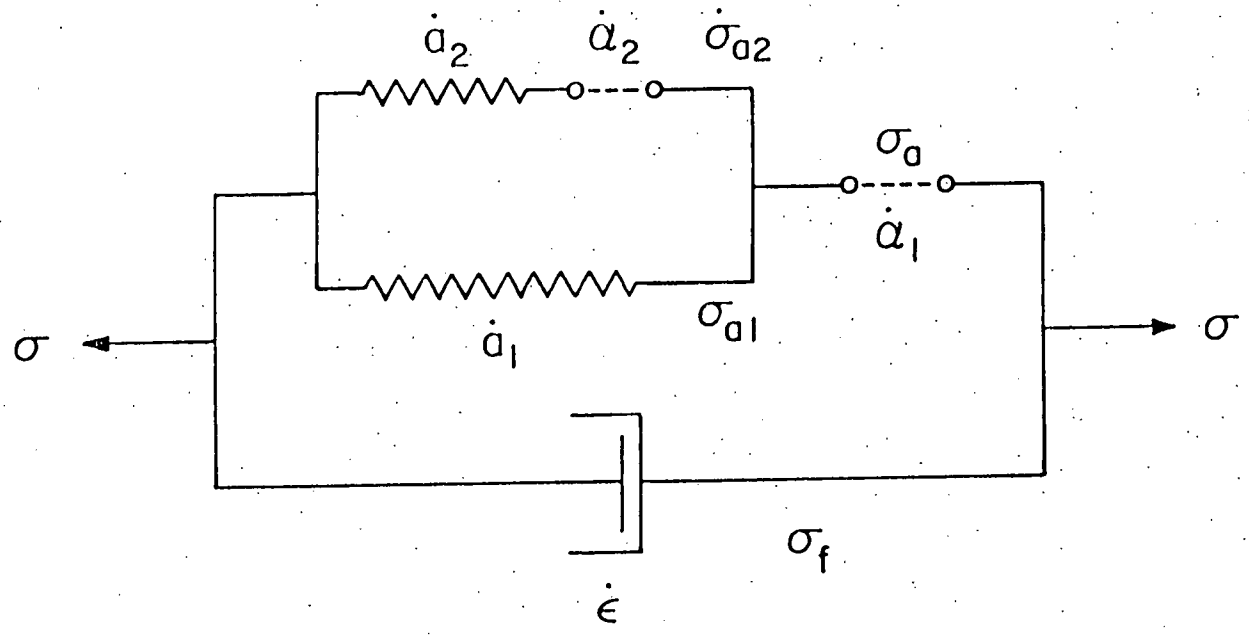

Figure 2: (a) A schematic representation of the new deformation model.

(b)

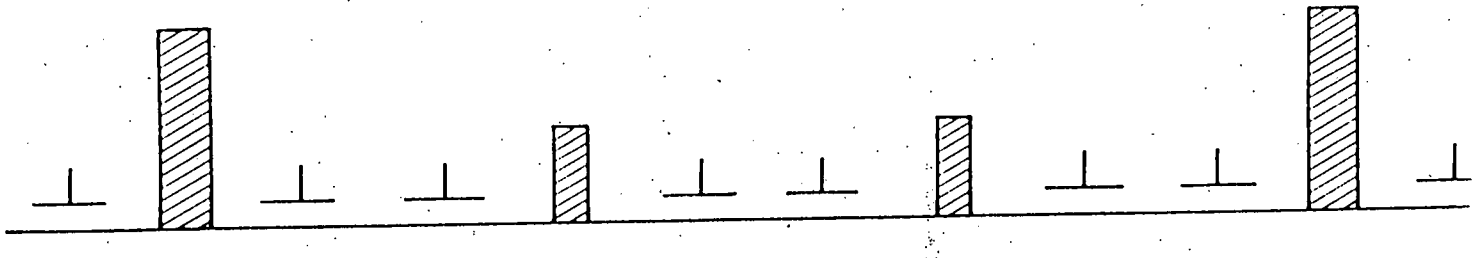

Figure 2: (b) A physical interpretation of the new model.

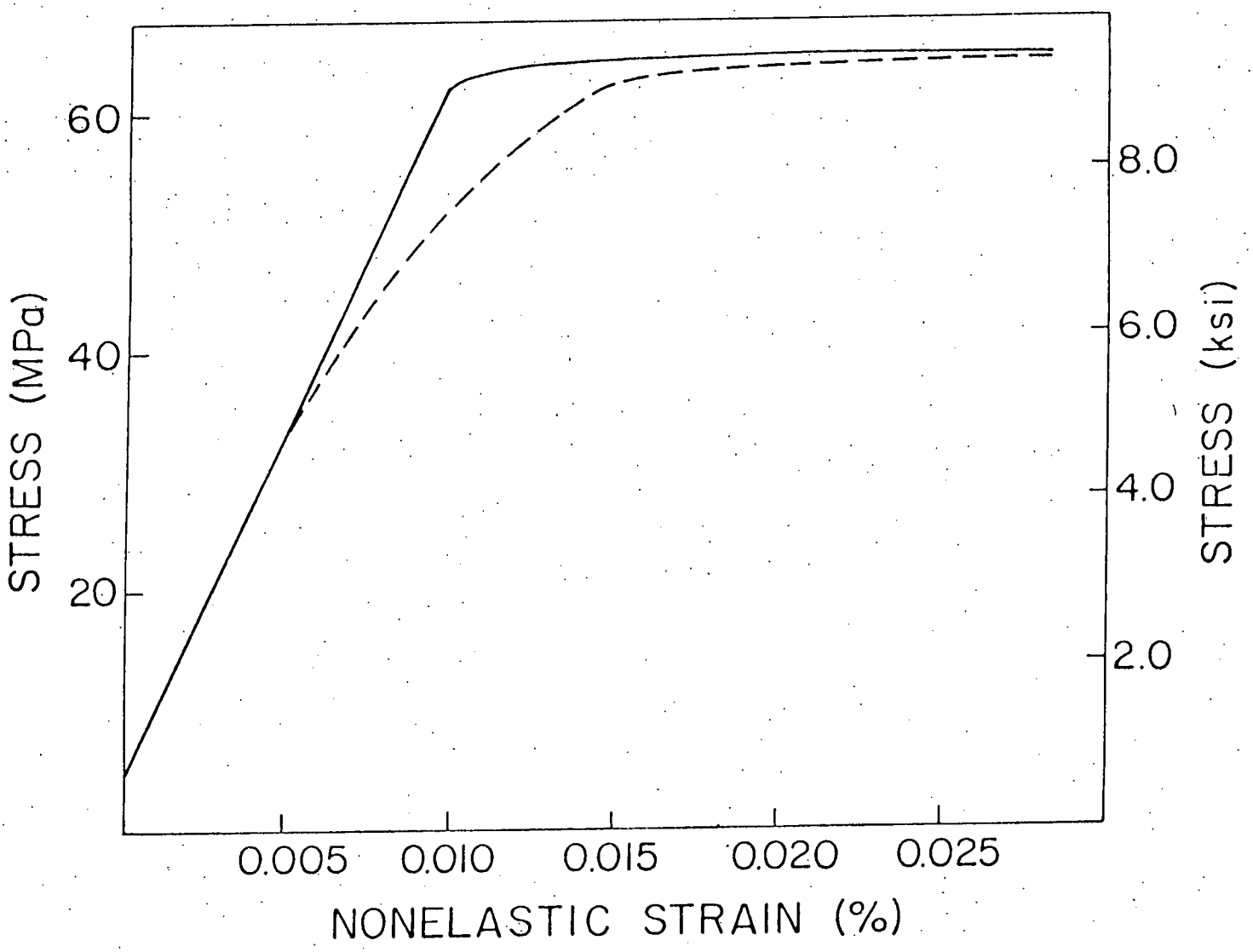

Figure 3: Computer simulation of a constant extension rate tensile test including plastic yielding. Hart's model: solid lines; new model: dashed lines.

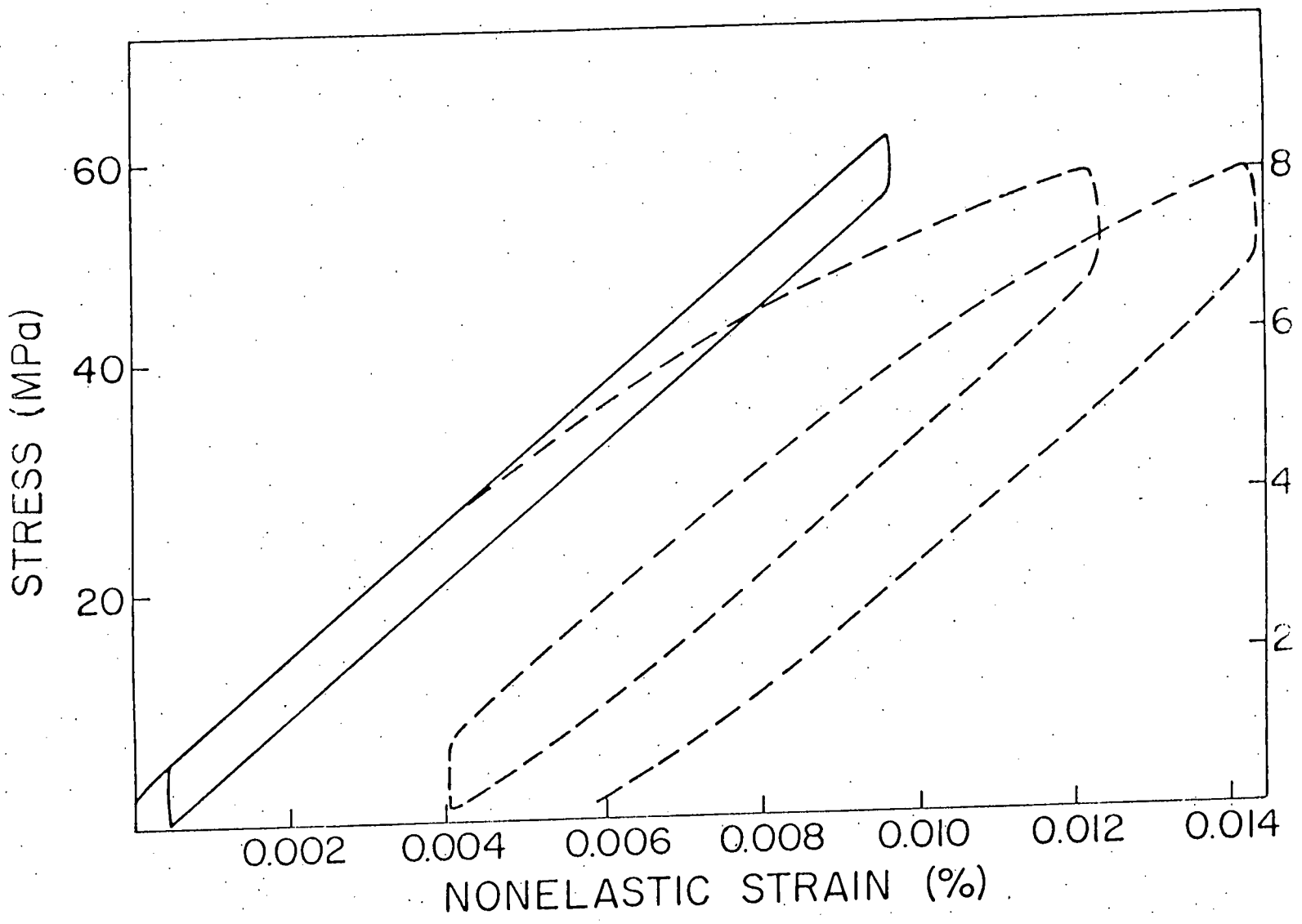

Figure 4: Computer simulation of loading and unloading loops below plastic yielding in a constant extension rate tensile test. Hart's model: solid lines; the new model: dashed lines.

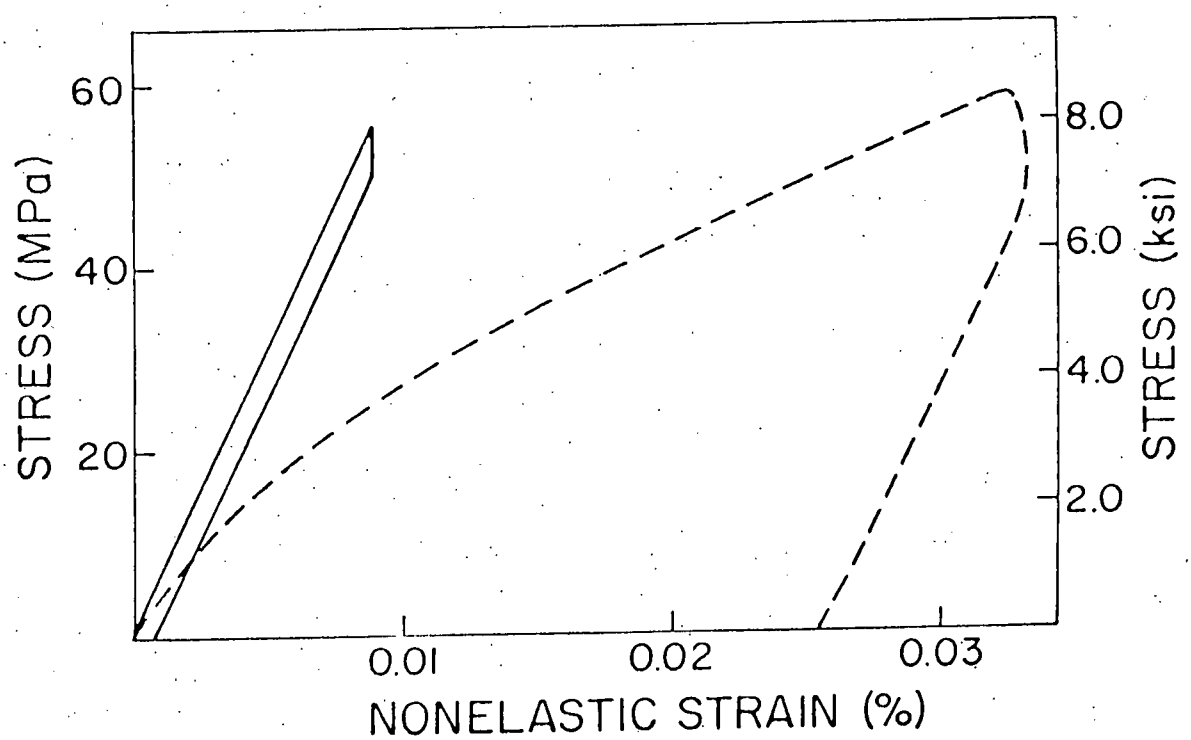

Figure 5: Computer simulation of the Bauschinger effect. The calculations shown are for loading in compression at a constant extension rate with a specimen which has been plastically deformed in tension. Hart's model: solid lines; the new model: dashed lines.

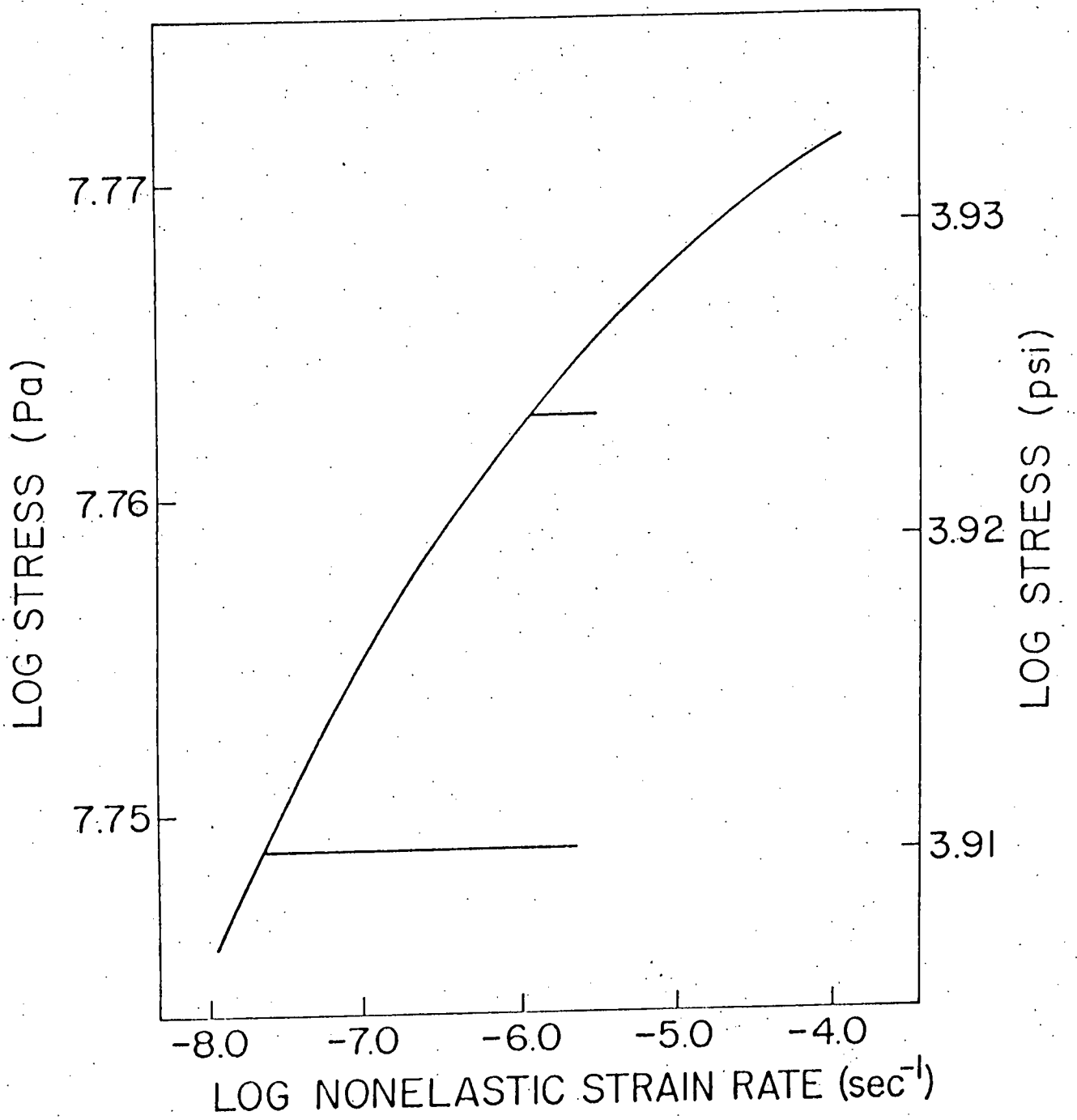

Figure 6: Computer simulation of load relaxation in the transient region.
(a) The upper most curve is the so-called "λ curve" (Equation 5) for relaxation by plastic deformation. The remaining curves are calculated for loading below plastic yielding prior to load relaxation. Hart's model: Figure 6a; the new model: Figure 6b.

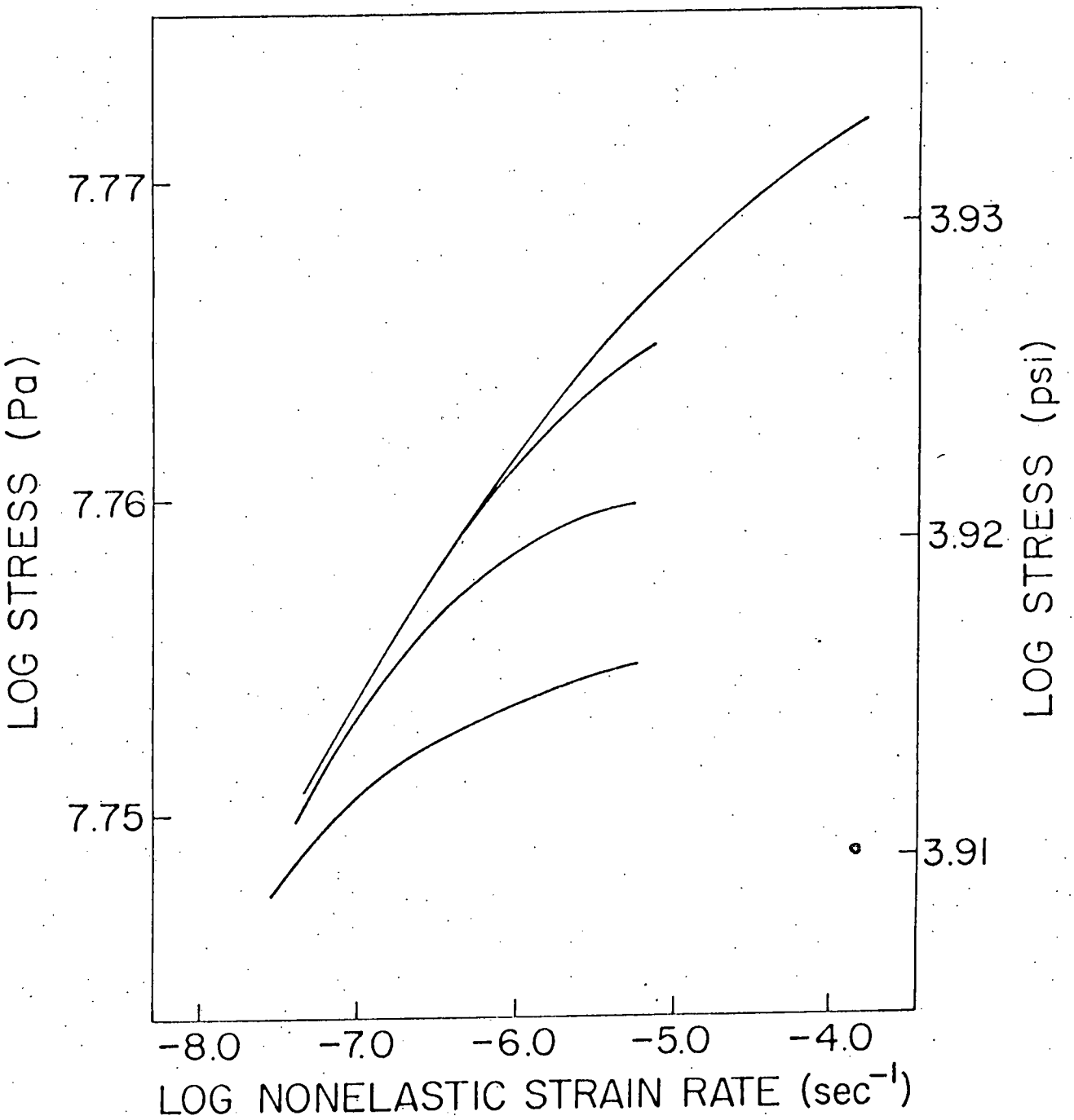

Figure 6: Computer simulation of load relaxation in the transient region. (b) The upper most curve is the so-called "λ curve" (Equation 5) for relaxation by plastic deformation. The remaining curves are calculated for loading below plastic yielding prior to load relaxation. Hart's model: Figure 6a; the new model: Figure 6b.

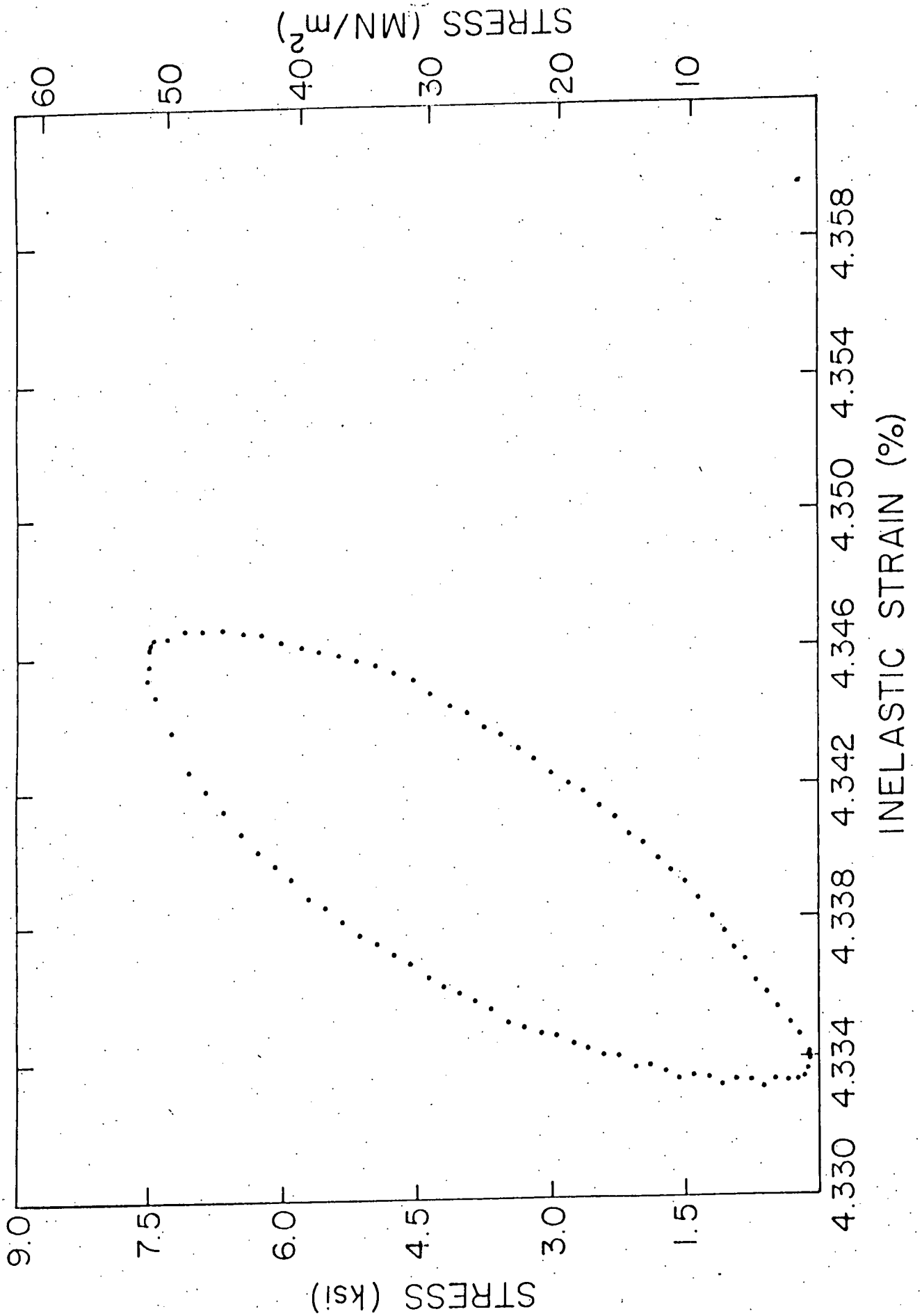

Figure 7: Experimentally determined loading-unloading stress-non-elastic strain loop for high purity aluminum at room temperature and an extension rate of 0.02 inch/min.

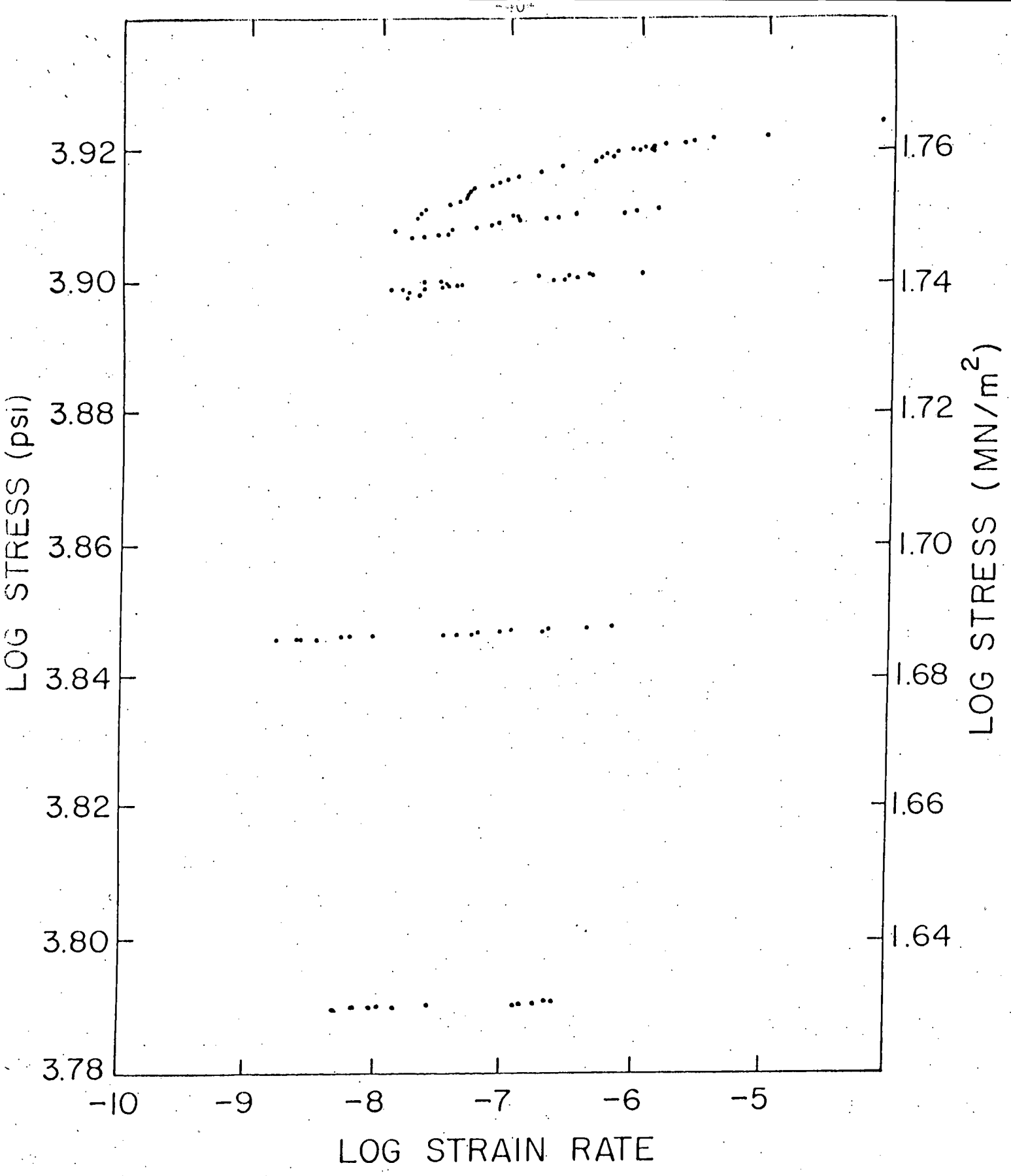

Figure 8: Experimentally determined transient load relaxation data similar to those shown in Figure 6 for a high purity aluminum at room temperature. The top curve is obtained in the plastic range.

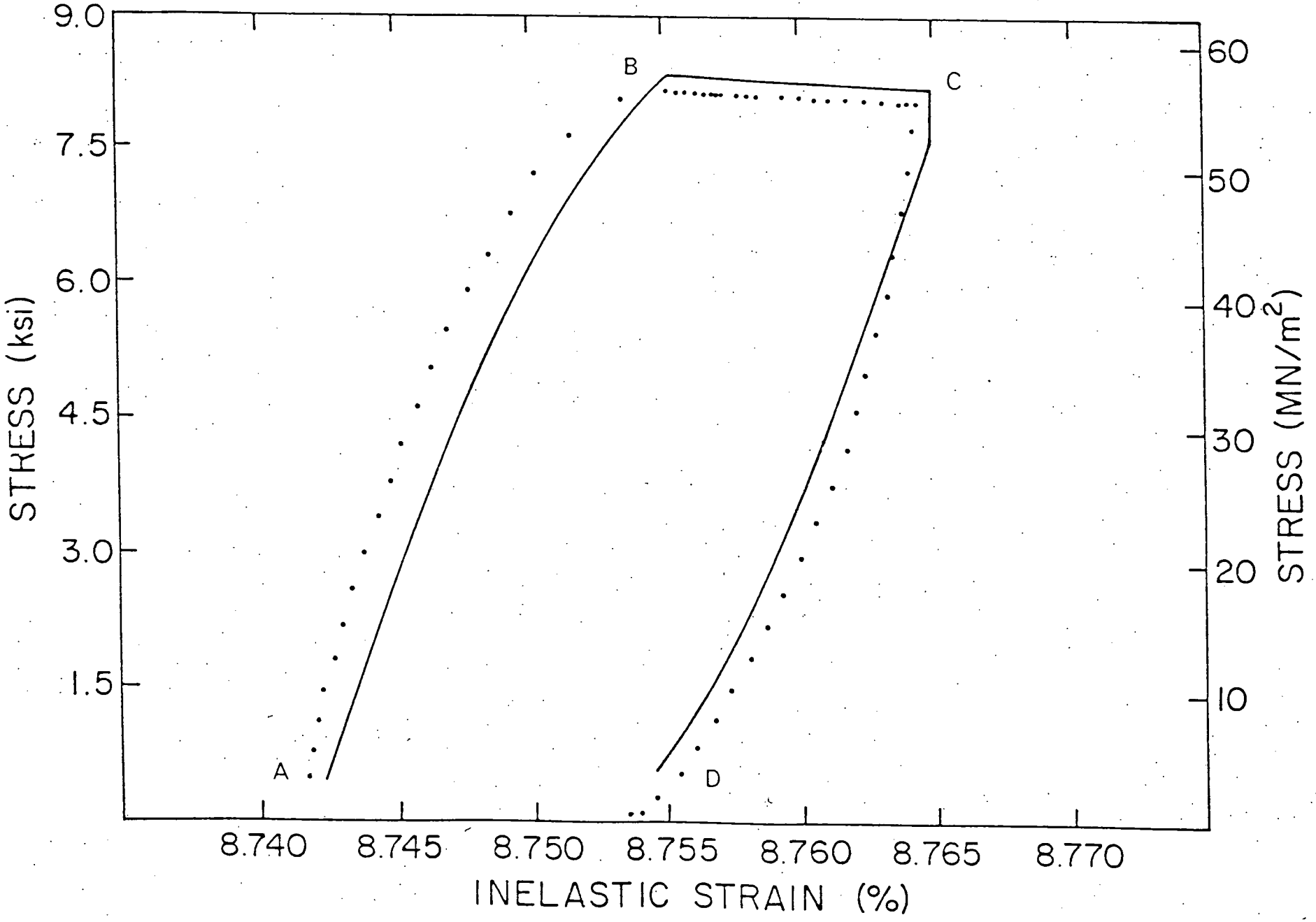

Figure 9: Comparison of experimental data and computer simulation by using the new deformation model; the parameters used are those in Table I; the experimental data are discussed in the text.

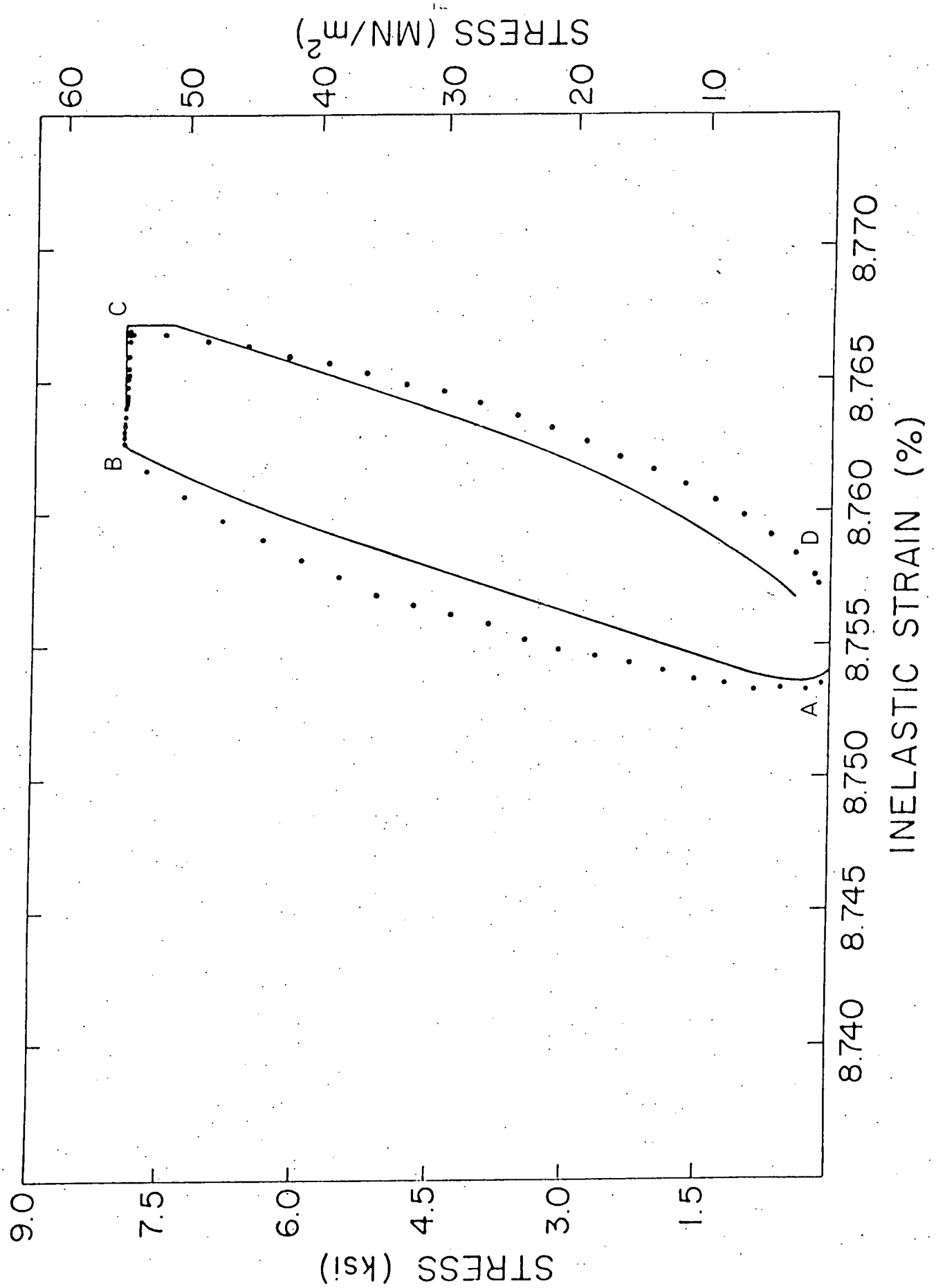

Figure 10: Comparison of experimental data and computer simulation by using the new deformation model; the parameters used are those in Table I; the experimental data are discussed in the text.

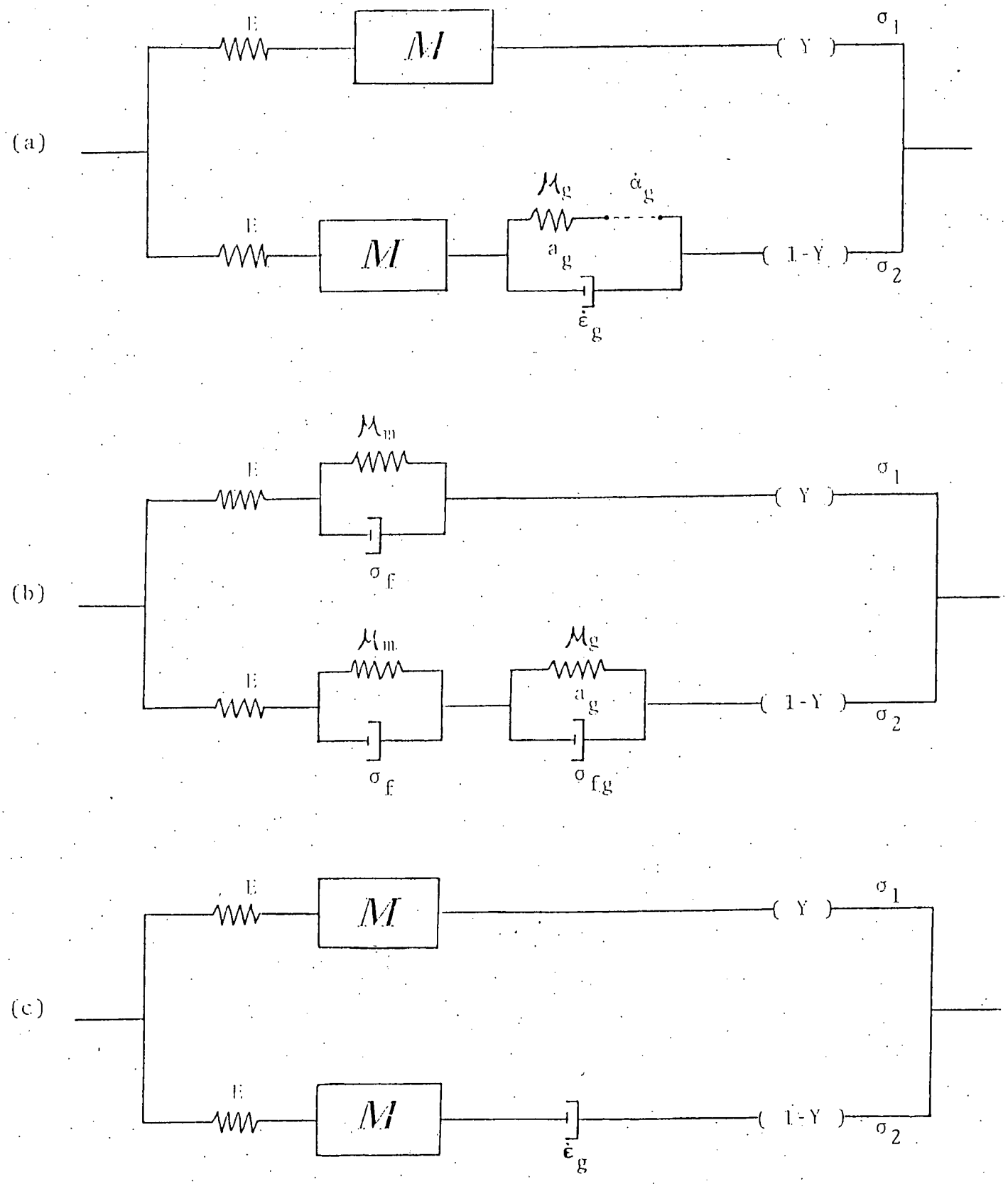

FIG. 11

Figure 11: A schematic representation of possible phenomenological models for grain boundary sliding.

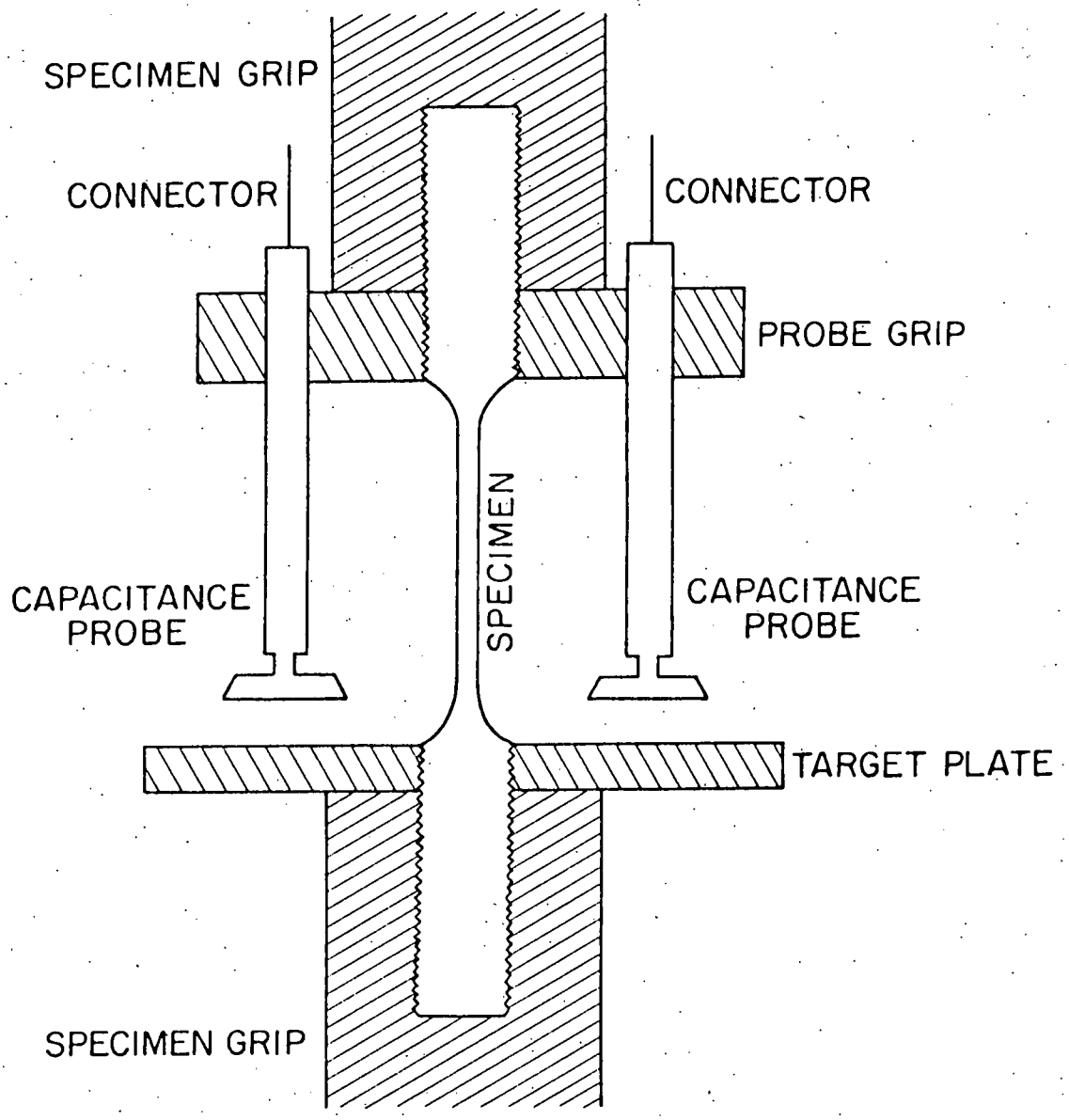

Figure 12: A schematic representation of capacitance gauge and tensile specimen assembly.

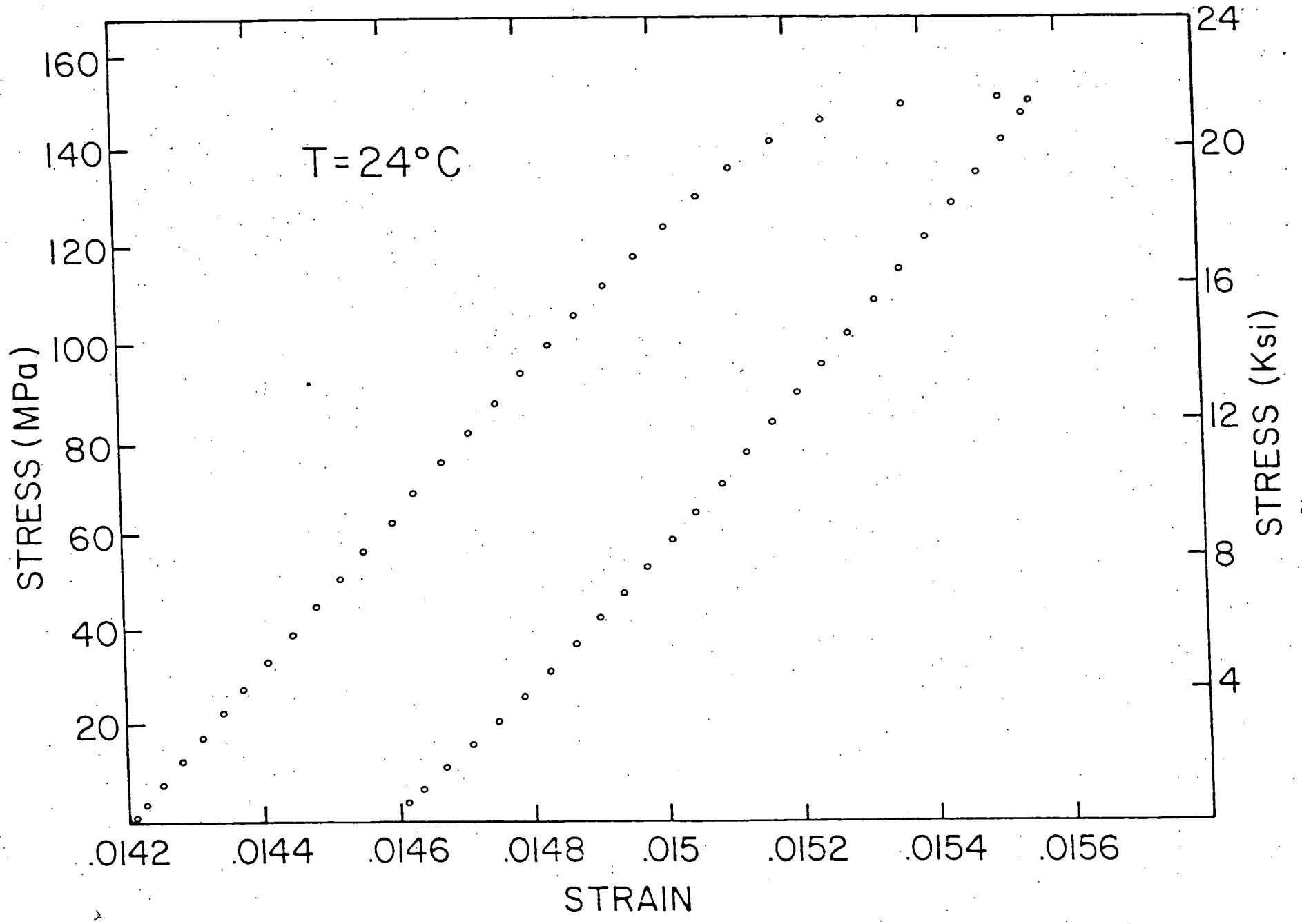

Figure 13: Room temperature, stress-total strain data obtained in a constant extension rate tensile test by loading-unloading in the microplasticity range (high purity aluminum and an extension rate of 0.02 inch/min.).

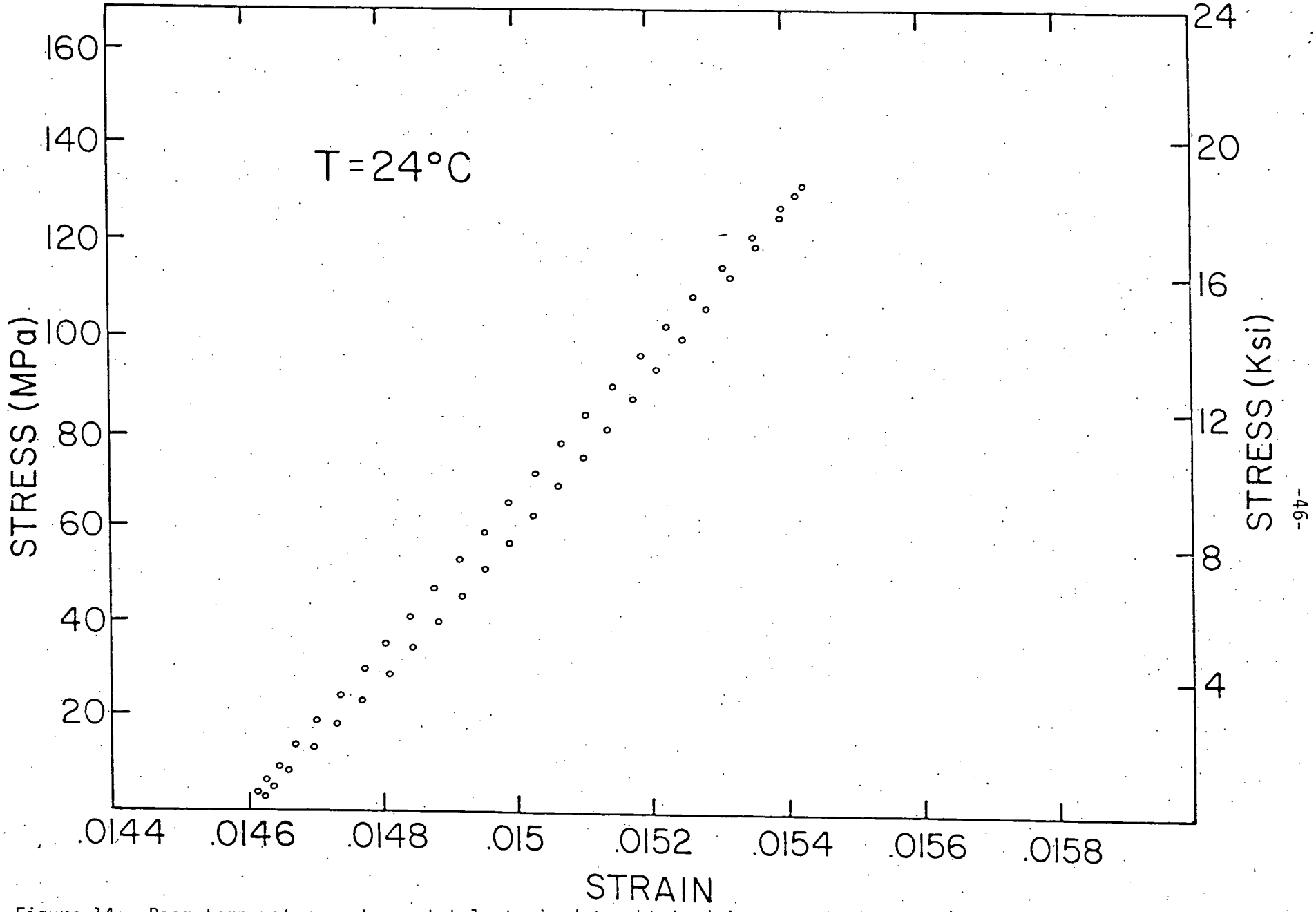

Figure 14: Room temperature, stress-total strain data obtained in a constant extension rate tensile test by loading-unloading with less microplasticity compared to the data in Figure 13 with the same experimental condition.

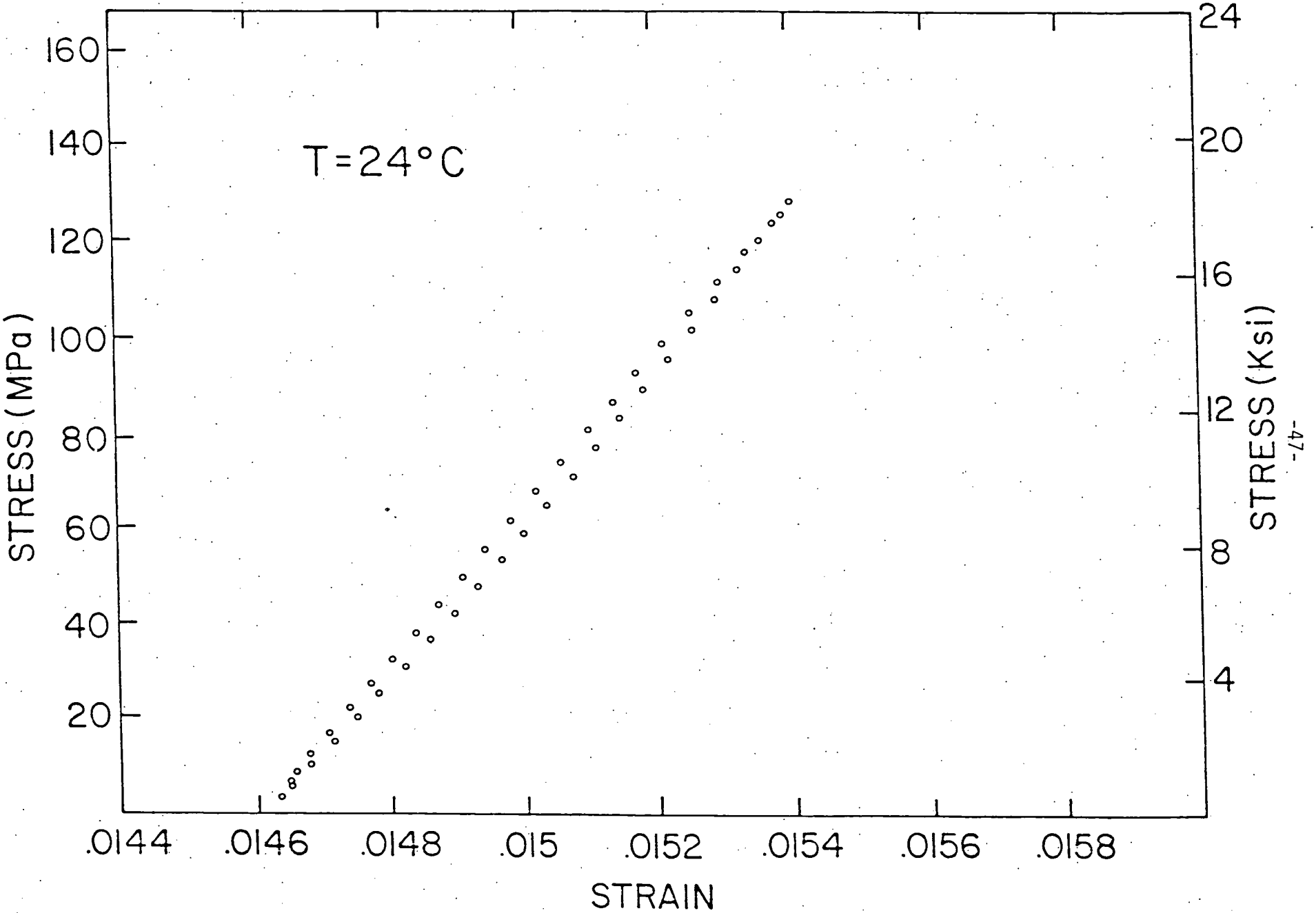

Figure 15: Room temperature, closed stress-total strain loop obtained in a constant extension rate tensile test by loading-unloading in the anelastic range with the same experimental conditions as those for the data in Figure 13.

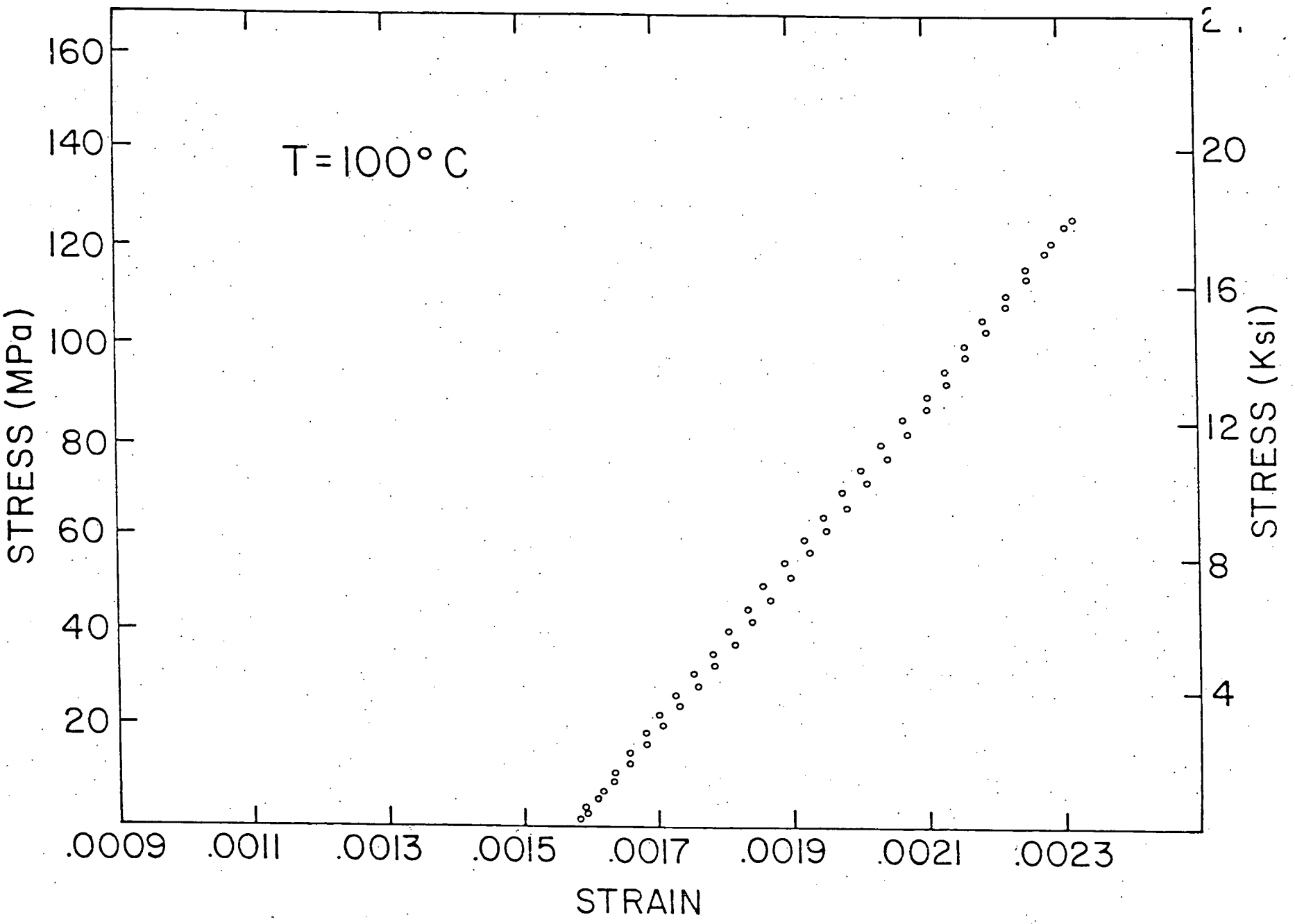

Figure 16: 100°C, closed stress-total strain loop obtained in a constant extension rate tensile test by loading-unloading in the anelastic range with the same experimental conditions as those for the data in Figure 13.

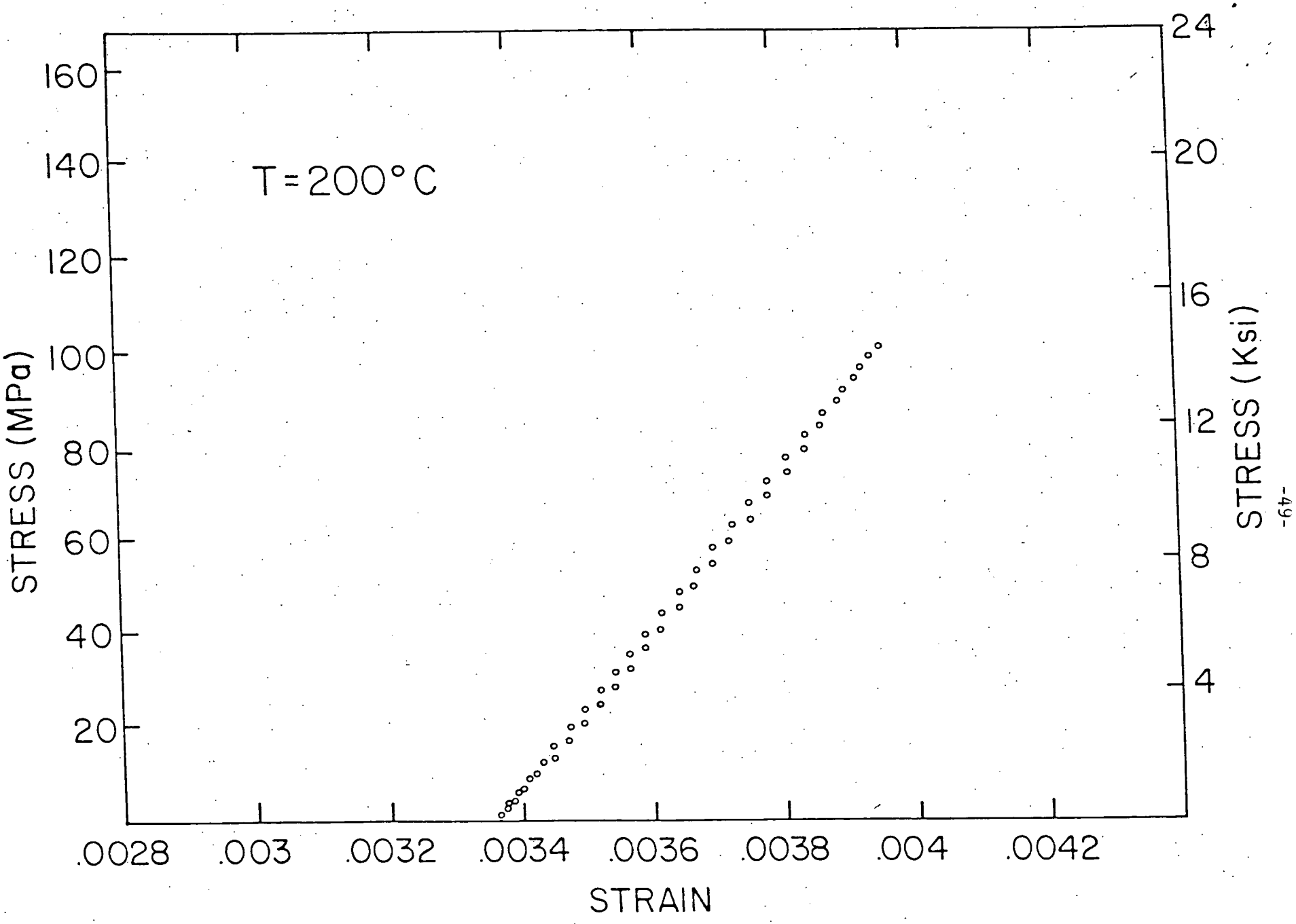

Figure 17: 200°C, closed stress-total strain loop obtained in a constant extension rate tensile test by loading-unloading in the anelastic range with the same experimental conditions as those for the data in Figure 13.

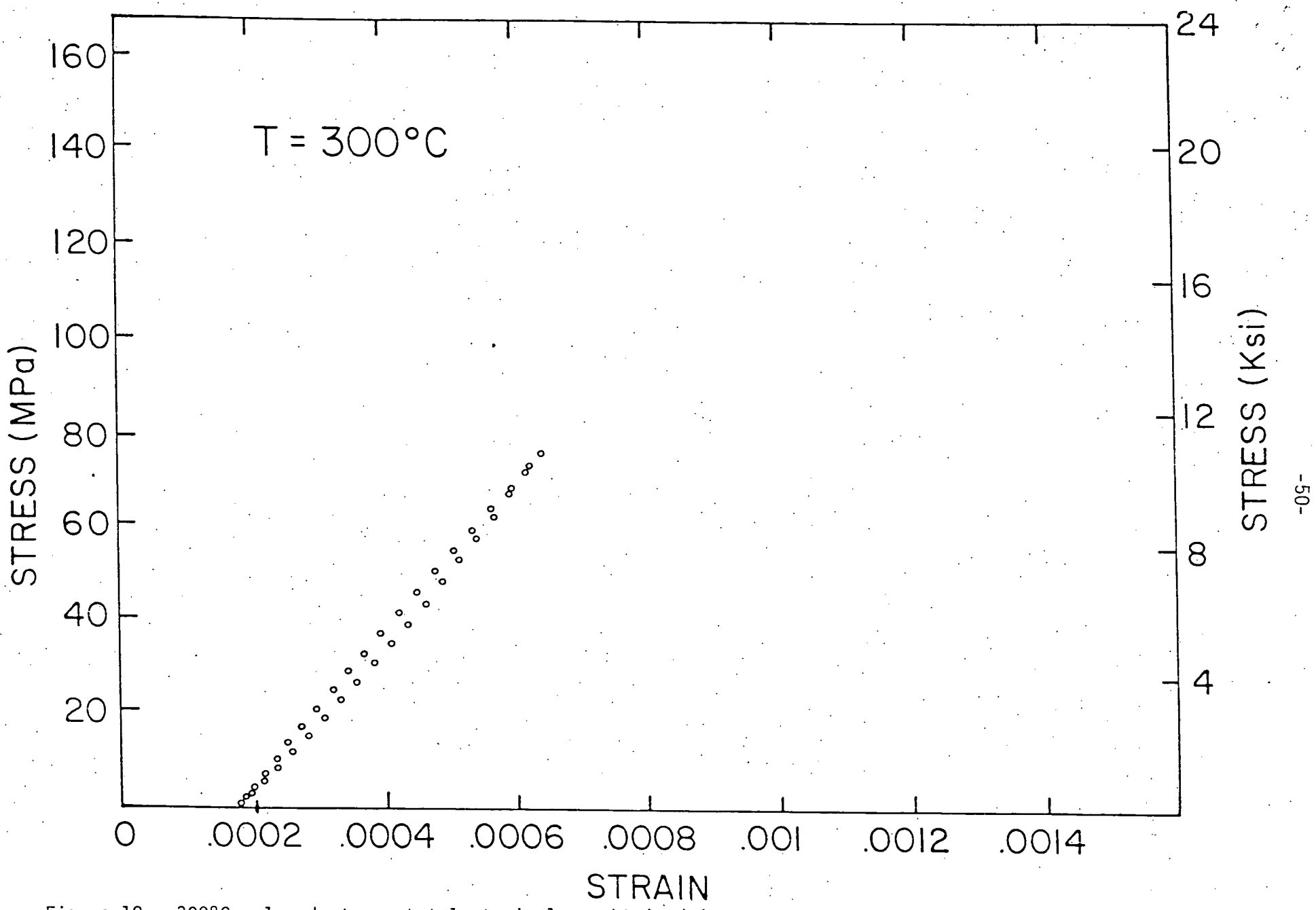

Figure 18: 300°C, closed stress-total strain loop obtained in a constant extension rate tensile test by loading-unloading in the anelastic range with the same experimental conditions as those for the data in Figure 13.

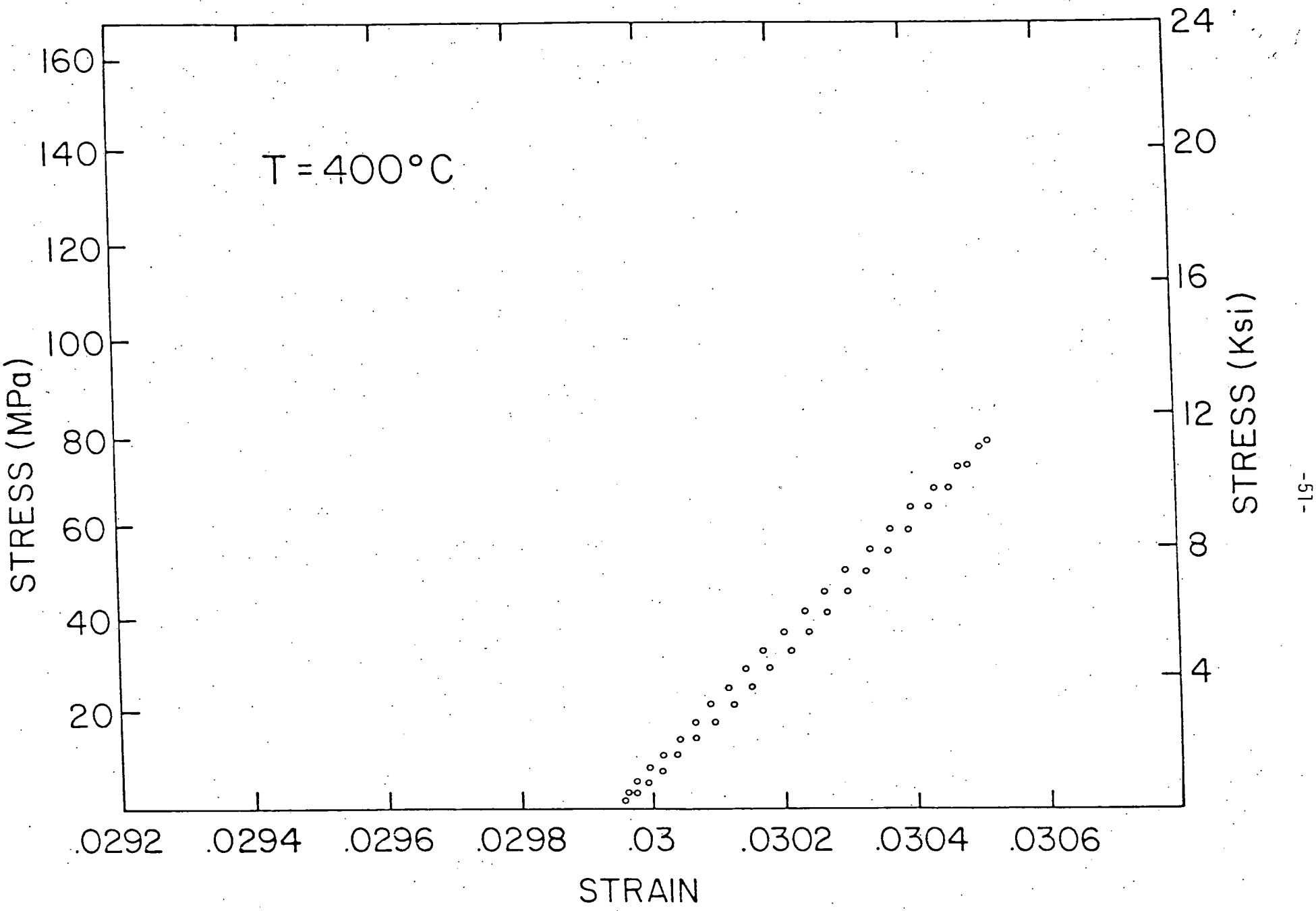

Figure 19: 400°C, closed stress-total strain loop obtained in a constant extension rate tensile test by loading-unloading in the anelastic range with the same experimental conditions as those for the data in Figure 13.

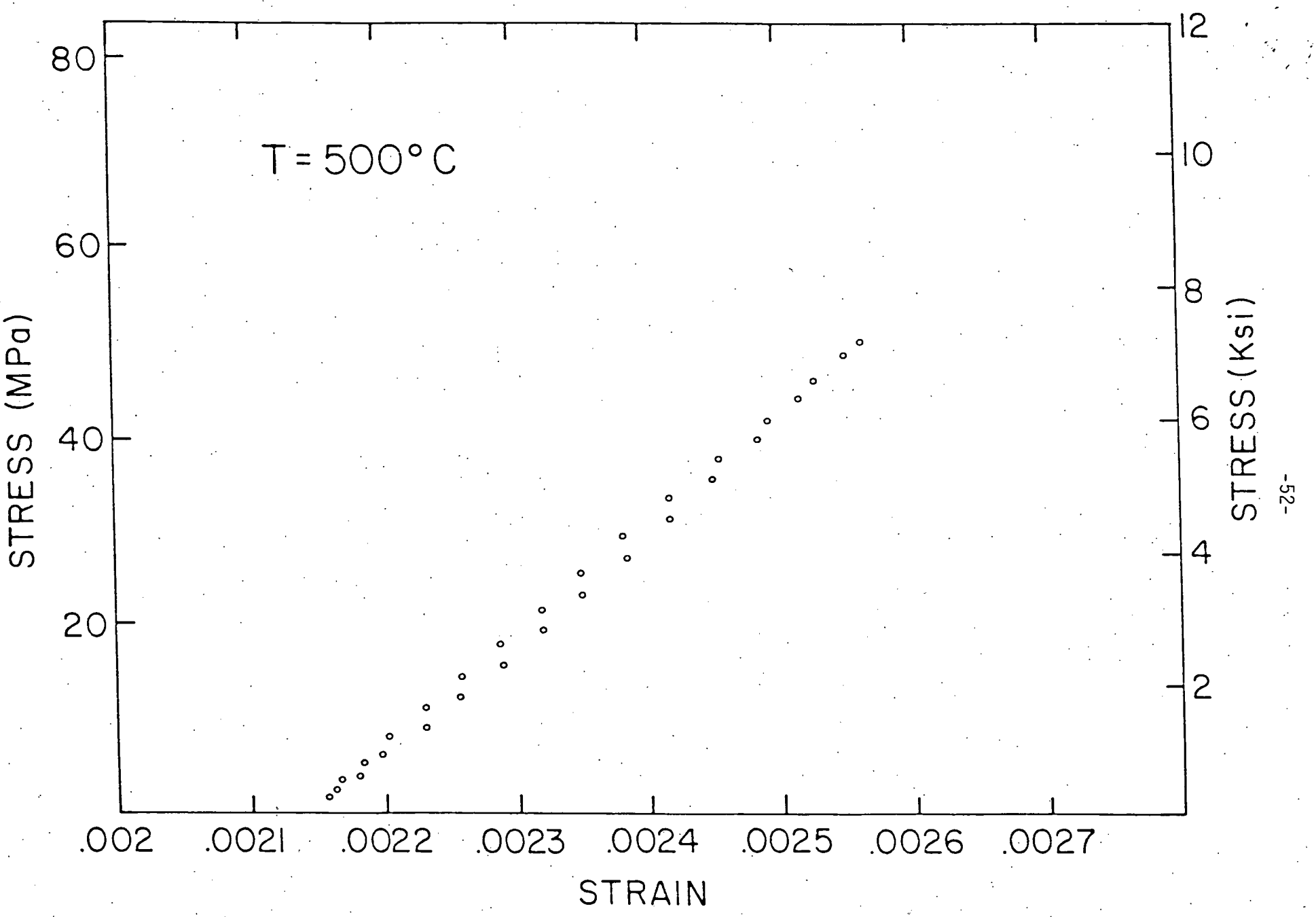

Figure 20: 500°C, closed stress-total strain loop obtained in a constant extension rate tensile test by loading-unloading in the anelastic range with the same experimental conditions as those for the data in Figure 13.

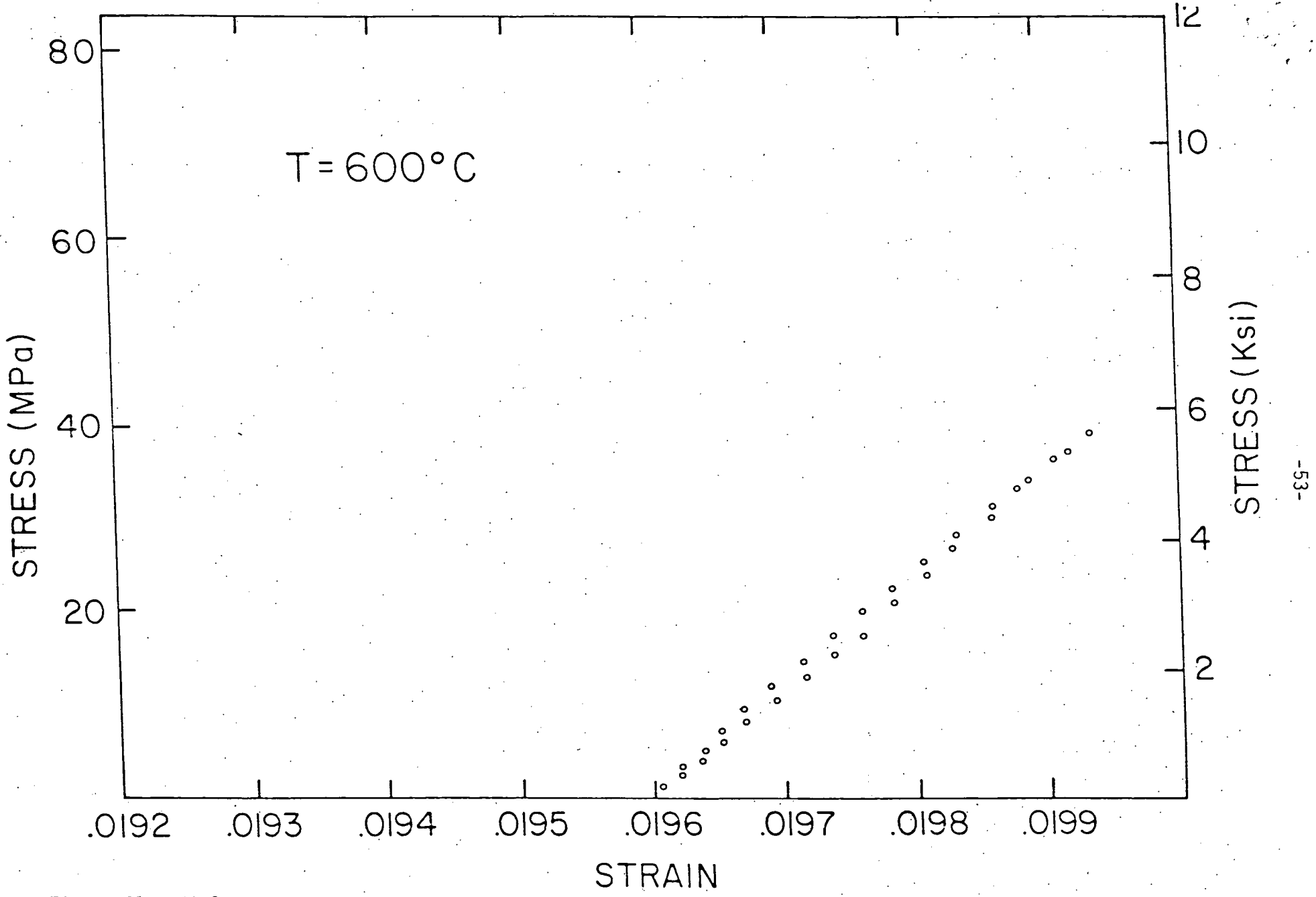

Figure 21: 600°C, closed stress-total strain loop obtained in a constant extension rate tensile test by loading-unloading in the anelastic range with the same experimental conditions as those for the data in Figure 13.

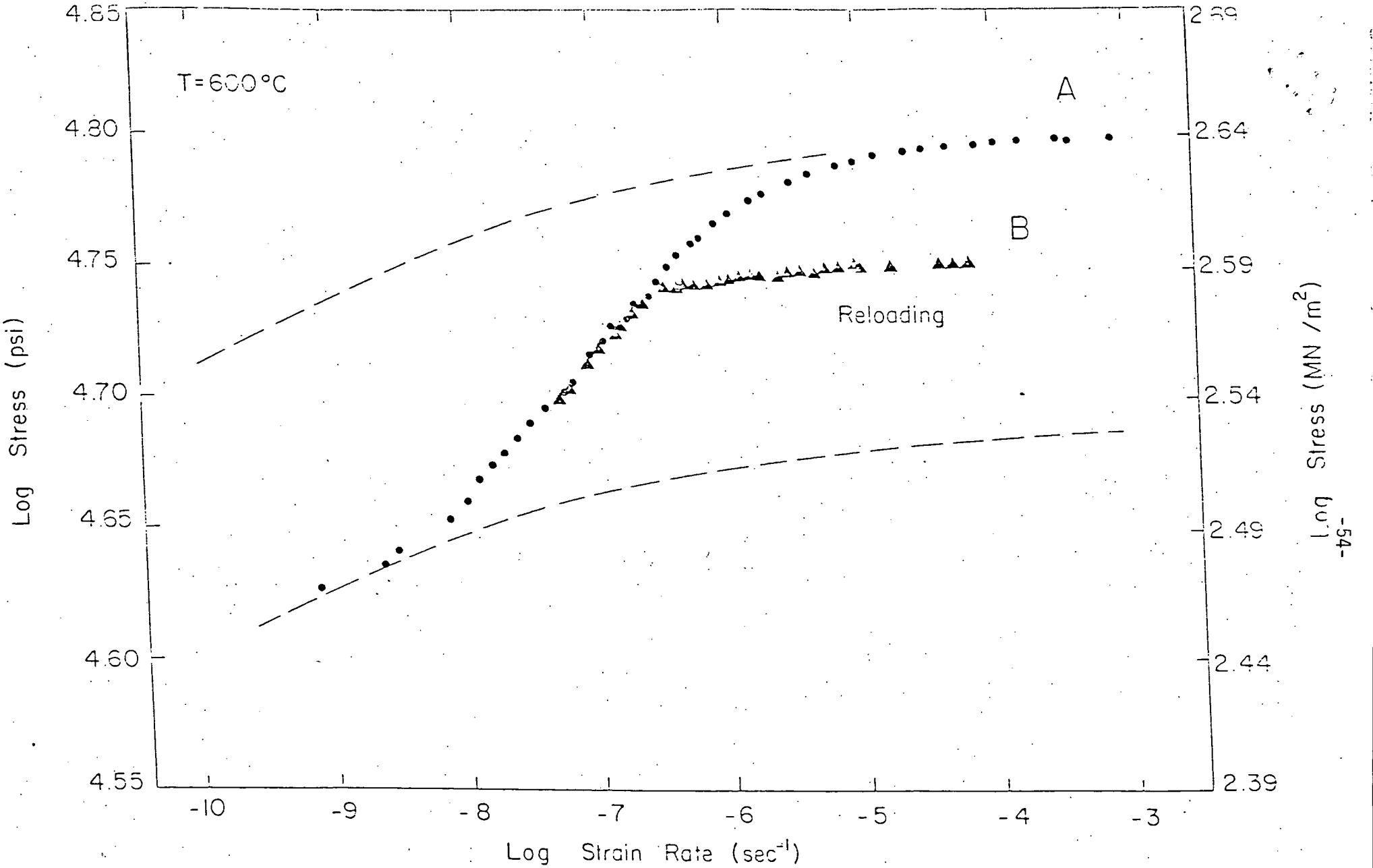

Figure 22: Load relaxation data of Type 316 stainless steel at 600°C in the plastic range showing the effect of grain boundary sliding (S-shaped curve). The two dashed curves represent two limiting grain matrix controlled relaxation conditions.

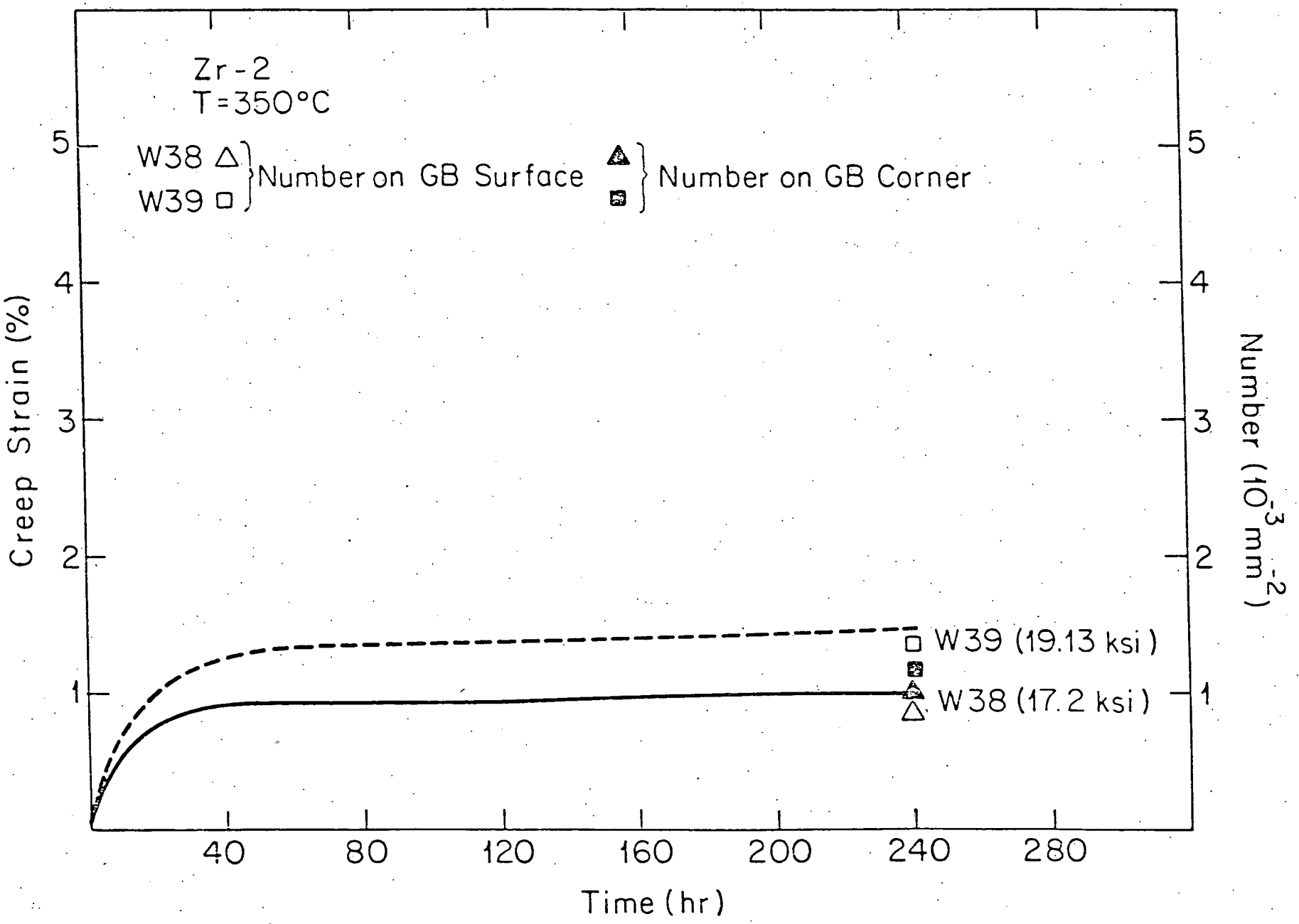

Figure 23: Measured number density of creep cavities in Zr-2 at 350°C in the same plot with the creep strain of the specimen.

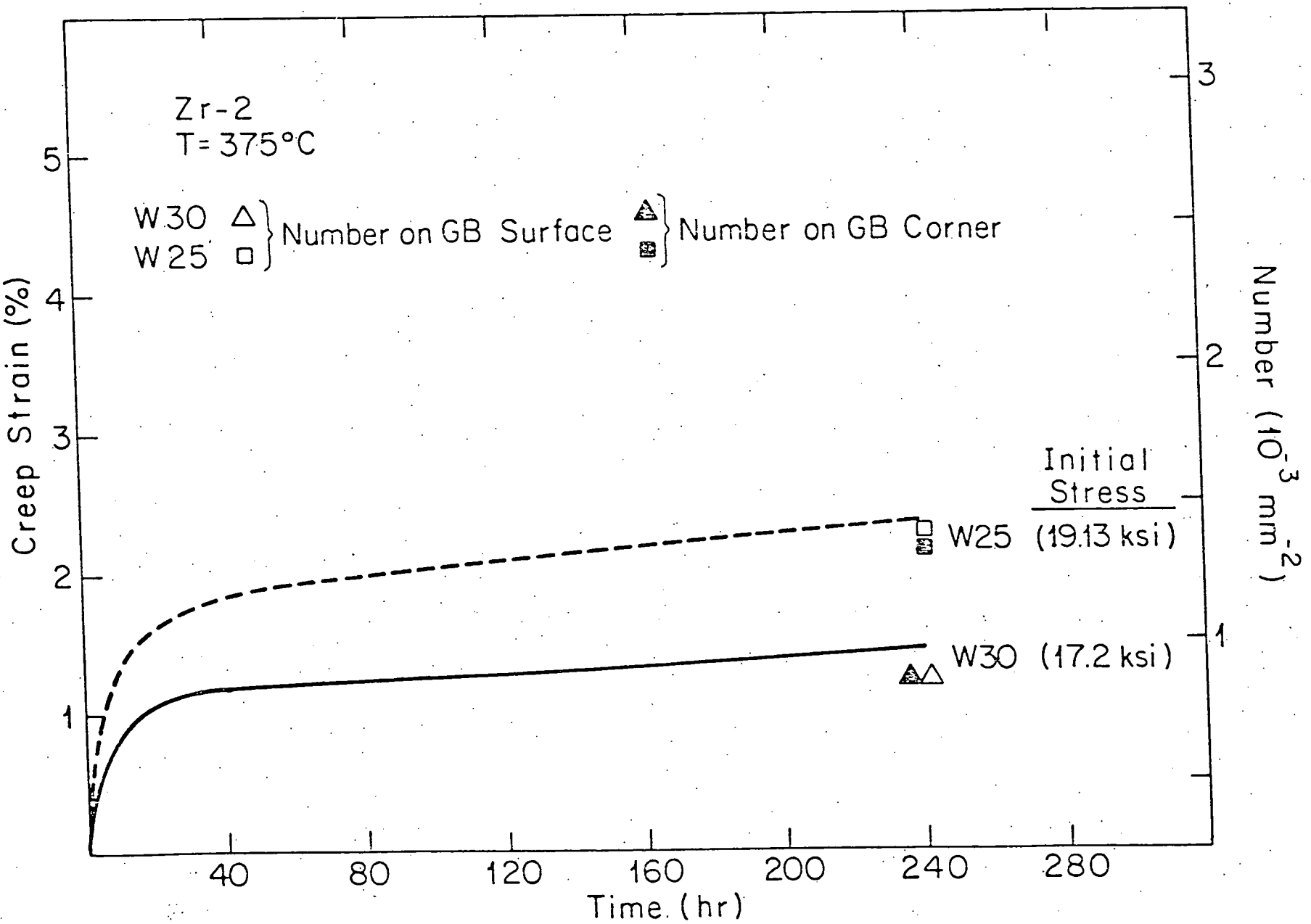

Figure 24: Measured number density of creep cavities in Zr-2 at 375°C in the same plot with the creep strain of the specimen.

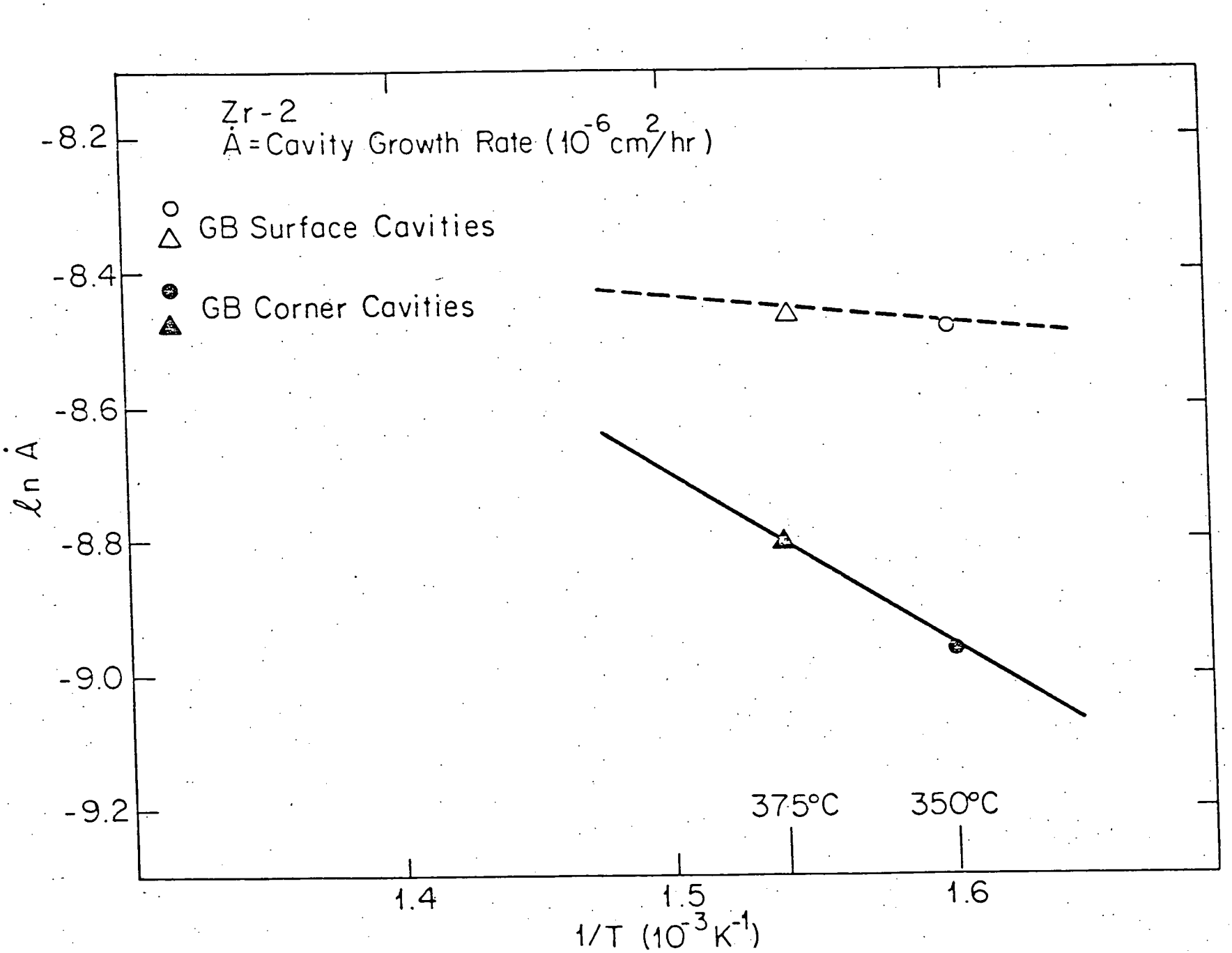

Figure 25: Logrithmic cavity growth rate plotted vs. 1/T. The growth rate is measured based on the cross-sectional area of the cavity. Applied stress is 17.21 ksi.